Politecnico di Milano

Scuola di Ingegneria dei Sistemi

Corso di laurea in Ingegneria Matematica

Finite Volume Electrohydrodynamic Simulations of Corona Discharge in Air

Relatori: Dr. Carlo de Falco

Dr. Nicola Parolini

Correlatori: Dr. Francesco Agostini

Dr. Ivica Stevanović

Tesi di laurea di:

Davide Cagnoni, matr. 752181

Anno Accademico 2011-2012

al mio carissimo nonno

Abstract

Convection is arguably the most widely used in industry among several modes of heat transfer. In the last few years, several attempts of enhancing the cooling ability of a fluid stream by means of applied electric fields have been made, and both experimental and numerical studies have been conducted on the matter. This work presents both affirmed and original models for the description of charged particles injection in fluids by corona discharge, describes a mathematical framework for the discretization and numerical approximation of the PDEs governing the electrohydrodynamic phenomena, and provides comparison of the numerical simulations performed with experimental data in order to assess the newly introduced discharge models.

Sommario

La convezione è assai probabilmente il più utilizzato in ambito industriale tra i modi del trasferimento di calore. Negli ultimi anni, sono stati fatti molti tentativi di incremetare l'efficacia del raffreddamento per convezione attraverso l'applicazione di campi elettrici, e l'argomento è stato studiato sia sperimentalmente che numericamente. Questo lavoro presenta modelli sia affermati che originali per la descrizione dell'iniezione particelle cariche nei fluidi attraverso l'effetto corona, descrive una struttura matematica per la discretizzazione ed approssimazione numerica delle EDP che governano i fenomeni di elettroidrodinamica, e fornisce un confronto delle simulazioni numeriche eseguite con dati sperimentali, allo scopo di validare i nuovi modelli di scarica introdotti.

Acknowledgements - Ringraziamenti

This thesis is based for the most part on the work developed during my internship in ABB Switzerland Corporate Research Center: I want to thank in particular my supervisors Francesco Agostini and Ivica Stevanović for giving me this great chance in the first place, and for the continuous help, advice and support they have given me. I also want to thank Thomas Christen and Bernardo Galletti for their help and advice, and all the other interns I met, way too many to list, who made me have the greatest time in Baden.

Grazie ai miei relatori Carlo de Falco e Nicola Parolini, senza il cui aiuto e i preziosi consigli mi sarei perso in innumerevoli occasioni.

Il ringraziamento più grande va alla mia famiglia, per avermi supportato (e sopportato, specialmente in quest'ultimo periodo) sempre, e per volermi bene nonstante i miei innumerevoli difetti.

Contents

Chapter 1

Introduction and motivation

Since the beginning of the industrial era, heat transfer has constantly been an important part of most industrial processes: it was at first the condensation of water in the vapor engine, later the control of chemical production, cooling of combustion engine, refrigeration and air conditioning, and since the late 20th century, the thermal management of nowadays ubiquitous semiconductor devices.

In most of these applications, there is need to draw thermal energy from one place and convey it to some other: if we take a computer chip as an example, the engineer is interested in extracting as much as possible of the thermal power produced by the chip, and transfer it to surrounding environment, in order to maintain the working temperature of the chip within a range that guarantees the best performance and reliability.

Several techniques can be employed for heat transfer: conduction, phase transition,

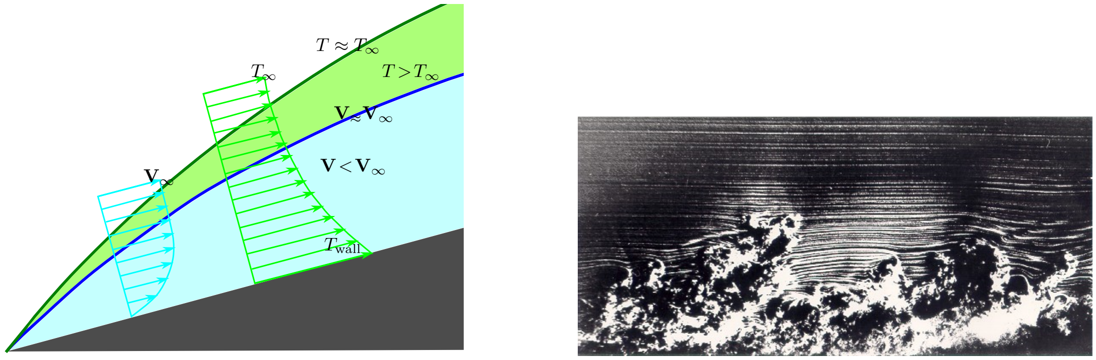

Figure 1.1: Left: theoretical representation of a boundary layer; right: experimental image of a boundary layer in turbulent regime.

natural or forced convection. In a vast majority of examples, the last step in the cooling process consists of transferring heat from some solid surface to the air in the surrounding environment.

Convective cooling refers to the transport of heat in a fluid by means of combined conduction, namely the diffusion of thermal energy, and advection, namely the motion of energy driven by the flow of the fluid. The latter contribution is predominant in bulk fluid, far from solid boundaries, but becomes negligible as one approaches walls or obstacles, where the velocity of the flow itself vanishes in the first place: this phenomenon is known as the formation of *boundary layers*, and is depicted in Figure 1.1.

Historically, most of the convective cooling systems are based on fans, used to drive the fluid flow over the surface of the device to be cooled. This approach is generally efficient, except for some applications with very specific requirements, for example:

- cooling of devices with highly localized “hot spots”, for which is unpractical to force a strong flow over the whole device to reduce the temperature of only a limited region,
- cooling of devices contained in enclosures that do not have enough room to place large fans,
- cooling by means of “dirty” air, containing some small objects or particles which could limit the durability of moving mechanical parts,
- applications for which mechanical vibrations or noise are to be avoided.

Recently, an alternative method for driving the flow of cooling fluid, namely the use of *ElectroHydroDynamics* (EHD) forces, has been exploited in many applications (see Fig. 1.2 and 1.3). In EHD, electric fields are applied in the fluid to accelerate charged particles. Impacts at the microscale between charged and neutral particles result at the macroscale in a volume force on the bulk fluid, creating or modifying its flow.

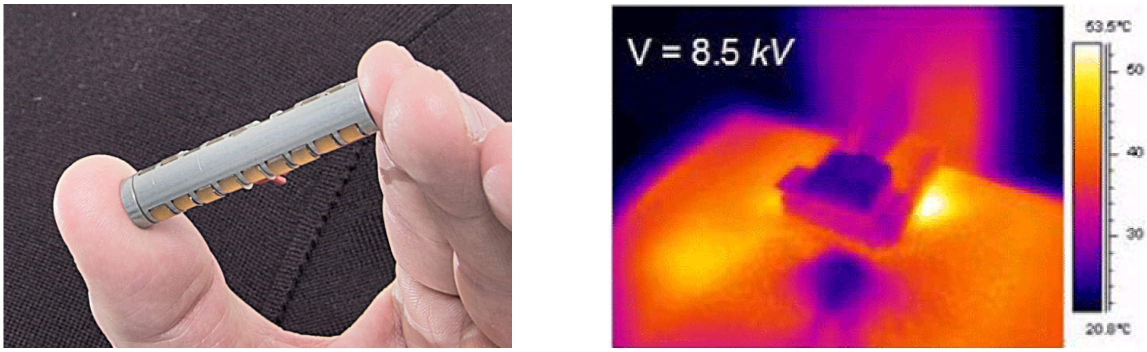

Figure 1.2: Left: EHD pump for cooling liquid, designed by NASA [46]. Right: Electrostatic fluid accelerator prototype from Tessera [29].

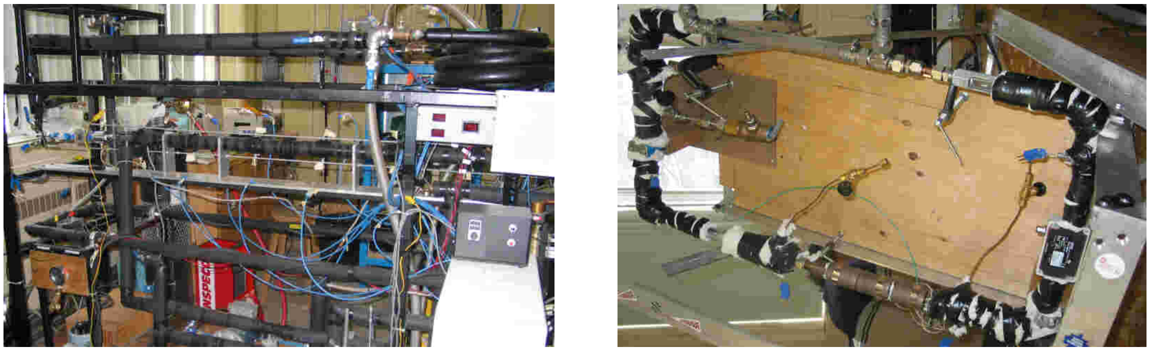

Figure 1.3: Facilities for experiments in EHD enhancement for boiling, condensation and capillary pumps at McMaster University [53].

In this thesis, we discuss the application of EHD and the production of charged particles for the enhancement of convective cooling in air, by disturbing and reducing the velocity boundary layers. Since the problem is approached by means of numerical simulations, the mathematical models and the algorithms for the solution of the related PDEs are also covered. In particular, existent and original lumped models for the prediction of charged particles generation are presented, implemented and validated.

1.1 Review of EHD enhanced heat transfer

In this section, we briefly review recent literature related to physical modeling of EHD phenomena, their application to heat transfer enhancement, and the numerical approximation of the governing equations.

EHD forces can be employed for heat transfer enhancement in two main ways. In cooling systems based on multiphase flow, EHD forces are used to initiate or enhance the formation of droplets or bubbles in the fluid; in cooling systems based on single-phase flow, EHD forces are used to accelerate free charged particles contained in the fluid.

Enhanced condensation or boiling was the first application to be exploited at industrial level, and has been studied extensively since more than thirty years (see, e.g., Jones' review [40]). Nonetheless, this approach is still currently employed and studied, for example by Cotton, Robinson and others [67, 16, 56].

Electrostatic fluid accelerators, on which we will focus in the following, are gaining an increasing appeal especially in semiconductor thermal management, thanks mainly to the promise of reduced dimensions of the cooling devices. Recent contributions in the field have been focusing on both numerical simulations and experimental studies:

- Adamiak and others [1, 7, 64, 65, 77] studied the DC and pulsed corona discharge between a needle and a plate collector, using different numerical methods (FEM, BEM, FCT etc.) for the approximation of each equation in the PDE system;

- Kasayapanand and Kiatsiriroat [44, 45, 43] simulated the effect of electrohydrodynamics in differently shaped channels by the finite difference method;

- Ahmedou and Havet [3, 2, 4] used a commercial FEM software to investigate the effect of EHD on turbulent flows;

- Moreau and Touchard [54], Huang and others [31], and Kim and others [47] experimentally studied different EHD devices designed for cooling or air pumping purpose;
- Chang, Tsubone and others [13, 73, 12] made extensive experimental study of the forced airflow and the corona discharge in a converging duct;
- Jewell-Larsen and others [42, 39, 38, 30, 36, 35, 37] and Go and others [25, 24, 22, 27, 26] conduced both experimental and numerical studies aimed at designing and applying ionic wind cooling devices to thermal management of cooling devices, and provided

The literature on the analysis of EHD equations is not very extensive: a few studies of the existence of a solution in 2D are carried out by Ryham in [63, 62]. Interesting analytic results can be found, however, in the literature on electrochemistry and flows in ionic solutions, which give rise to inherently similar equations, namely the Navier-Stokes-Poisson-Nernst-Planck system (see, e.g., [61, 34]). We refer, for example, to the work of Jerome, Sacco and others [8, 14, 50, 49, 32, 33].

1.2 Contents and scope of this thesis

The main focus of this thesis work is the formulation and implementation of an algorithm for the numerical simulation of single-phase EHD cooling systems. The requirements for obtaining an industrially interesting tool are that the simulations should be acceptably matching experimental results, and have a certain degree of prediction ability. In this case, numerical simulation can be used as a first step in the design of actual devices, without the need of immediate experimentation in the first stages of the designer's work. This thesis is structured as follows:

Chapter 2 presents the physical description of the phenomena which govern the electrohydrodynamic cooling, along with the mathematical models necessary to its description:

- in Section 2.1, the different possible interactions between electric fields and charged fluids are reviewed, and a mathematical formulation for the EHD force on ionized air is provided;
- in Section 2.2, the partial differential equations which govern the electrohydrodynamic phenomena are introduced, and the couplings between the equations are clarified;
- in Section 2.3, the physics of electron avalanche in corona discharge is analyzed, and successively different boundary lumped models for the discharge is proposed, some of which for the first time;
- in Section 2.4, the differential and boundary models are completed with boundary conditions, in order to provide the formulation of an initial-boundary-value differential problem.

Chapter 3 concentrates on the algorithmic aspects of the numerical simulations, with the final purpose of transforming the original PDE system in a set of linear algebra problems:

- Section 3.1 reformulates the problem as a discrete dynamical system on proper function spaces;
- Section 3.2 provides a first decoupling of the differential equations in subproblems, and introduces an iterative algorithm for computing the solution at each time step;
- Section 3.3 introduces a modified and linearized version of the electrical problem, and delineates an iterative algorithm for its solution;

- Section 3.4 introduces the finite volumes method for PDEs discretization, and provides a general space-discrete formulation for the linearized problems;
- Section 3.5 presents the solution method for fluid dynamics subproblem, based on the space-discrete formulation.

Chapter 4 presents the results of numerical simulations obtained through the implementation of the described algorithm, and compares the results with experimental and numerical works on EHD present in literature, along with a comparison and validation of the different lumped models proposed in Section 2.3.

Chapter 2

Physics of electrical discharge in gases

Electrical discharge in gases can occur in several different regimes, involving very different physical phenomena. Charge carriers can be externally injected as charged droplets, small particles, or ionized gas molecules, or they can be generated by ionization of the gas itself, when excitation inducedby the electric field in gas particles is sufficient to break molecular bonds. In such situations, the properties of the gas may be radically changed, and the gas itself may be turned into plasma in part of the system.

A particularly effective approach for introducing charges in the system consists of exploiting the so called *Townsend avalanche* process, i.e., avalanche multiplication of free electrons by impact-ionization of neutral gas molecules. In order for this process to be triggered, free electrons traveling through bulk gas under the effect of an externally applied electric field, must gain in one free flight period a kinetic energy higher than the gas ionization energy.

When this situation occurs, an ion-electron pair is produced by each collision and the newly generated charges, in turn accelerated in the electric field, contribute to more ionizing impacts and lead to an avalanche. When a large number of free carrier pairs is generated in a globally neutral gas, one can say the gas has been turned into a plasma.

The region occupied by the plasma may have a large extent if the electric field is overall uniform, but by a proper geometric design of the electrodes one can constrain it to a thin

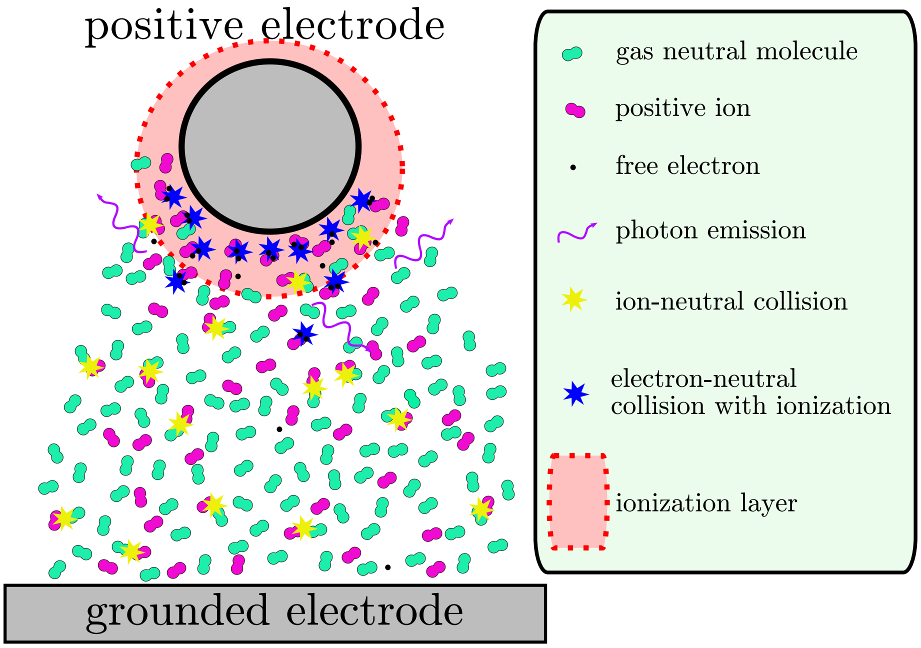

Figure 2.1: Out-of-scale depiction of the positive corona discharge in gas.

layer. For example, a sharp anode (a pin, or a really thin wire) will produce a strong electric field in its proximity; electrons generated within this high field region will be attracted and quickly captured by the positive electrode, while cations will have to travel trough the low electric field, or "drift", region to reach the cathode. Due to this difference, charge carriers can be considered as unipolar in the bulk fluid, as is pointed out in [5]. The choice for the ionizing region to be near the anode is not arbitrary, but has some non negligible advantages: first, in the drift region only one kind of carrier is present, namely positive ions, whereas one would possibly have negative ions *and* electrons when ionizing near the cathode; second, the ozone production in the former case is much less than in the latter (see [11]), with obvious advantages in terms of air quality and material durability.

In this particular regime, known as *corona discharge*, the analysis can concentrate on the drift region, namely the fluid outside the ionization layer. In this region, fluid properties are reasonably uniform and a macroscopic modeling approach can be taken: i.e., ion number density, charge density can be modeled as continuous functions, and current density can be expressed as function of the electric field, the charge density and the *ion mobility* in the gas. Figure 2.1 depicts a system with the properties described above.

For very simple geometries one may apply further simplifications to the physical description introduced above. In particular, for a cylindrical metal pipe with a very thin coaxial emitting wire one can derive the two-parameter Townsend model (see Sect. 2.3) from which, in turn, a simple compact relation describing the current-voltage characteristic can be derived ([48, p.485-504]):

$$i \propto V(V - V_{\mathrm{on}}), \tag{2.1}$$

where i denotes the contact current, V the anode-to-cathode voltage and V_{on} is the “onset” voltage. For more complex geometries, a full PDE system including a drift-diffusion model for ion transport, Poisson equation for self-consistent electric field computation, and Navier-Stokes equations for the fluid velocity field in the bulk fluid is required. The development of such full model occupies the remainder of the present chapter. It must be noted, though, that relation (2.1) can still be useful for obtaining rough estimates of current, when the corona is in its fully developed, stable regime, i.e. when the condition $V \gg V_{\mathrm{on}}$ holds (see Figure 2.2).

The remainder of this chapter is structured as follows:

- Section 2.1 provides a detailed description of the model for EHD force,
- Section 2.2 describes the whole system of equations governing the bulk fluid and current flow,
- Section 2.3 introduces microscopic and macroscopic models for describing corona

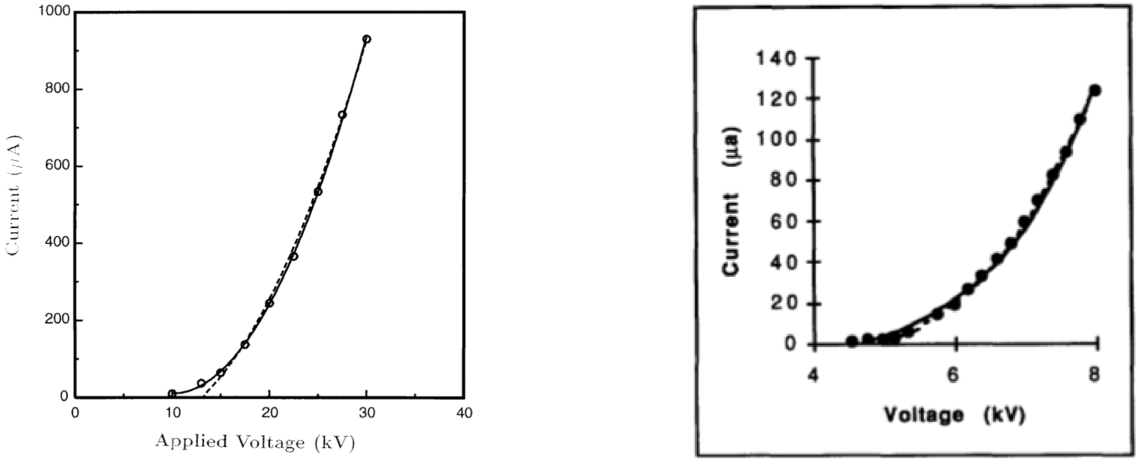

Figure 2.2: Examples of parabolic I-V characteristic as found in [55] (left) and [66] (right)

discharge,

- Section 2.4 summarizes the whole model and formulates the initial-boundary-value PDE problem.

2.1 Modeling of electrohydrodynamic forces on the gas

In this section, we describe the different kind of EHD forces. A fluid medium immersed in an electric field generated totally or partly by free charge carriers in the fluid, is subject to a volume force $\mathbf{f}_{\mathrm{EHD}}$ which can be expressed as the sum of four contributions:

$$\mathbf{f}_{\mathrm{EHD}} = \mathbf{f}_1 + \mathbf{f}_2 + \mathbf{f}_3 + \mathbf{f}_4, \tag{2.2}$$

where $\mathbf{f}_1$ denotes the contribution called Coulomb or electrophoretic force, $\mathbf{f}_2$ the permittivity gradient force, $\mathbf{f}_3$ the dielectrophoretic force and $\mathbf{f}_4$ the electrocostriction force. These four forces are functions of the number density of carriers in the fluid N_{p}, the electric field vector $\mathbf{E}$, the dielectric permittivity ε and the density of the fluid ρ .

In the following paragraphs, the four different terms in evidence in (2.2) will be discussed, based on the analysis presented in [68, p.96,137-40], [40] and [75].

Coulomb or Electrophoretic Force

The first contribution to EHD force represents the Coulomb force exerted by an electric field upon free electric charges in the medium, and it is also referred to as electrophoretic force:

$$\mathbf{f}_1 = qN_\mathrm{p}\mathbf{E};$$

$\mathbf{f}_1$ is not negligible when there are free charges either flowing in the fluid or building up at the interfaces of two fluids due to variations in permittivity and conductivity. The first situation occurs for example when the already introduced corona discharge generates a current flowing through the fluid; the second case occurs in instance multiphase flows: the steep gradients in electrical permittivity ε and ion mobility μ can cause the building of large amount of carriers, of which an estimation is given in [6] :

$$\mathbf{E} \cdot \nabla\varepsilon = qN_\mathrm{p} + \frac{\varepsilon}{\mu N_\mathrm{p}}\mathbf{E} \cdot \nabla(\mu N_\mathrm{p}).$$

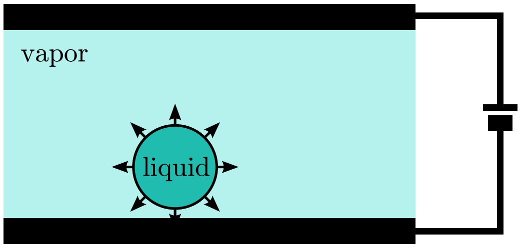

Figure 2.3: Effect of $\mathbf{f}_2$ upon droplet formation [75].

Permittivity gradient force

The second contribution in EHD force is driven by the spatial gradient of permittivity $\nabla\varepsilon$:

$$\mathbf{f}_2 = -\frac{1}{2}|\mathbf{E}|^2\nabla\varepsilon.$$

This term is particularly important in two-phase heat transfer processes where the fluid permittivity changes significantly at the vapor/liquid interface. The direction of the resulting force is thus from the more permittive material (liquid) towards the less permittive (vapor) and is normal to the interface. This component of the force acts to disturb condensate films and deform liquid droplets as shown for instance in Fig. 2.3.

Dielectrophoretic Force and Electrostriction Force

The third and fourth contribution to EHD force are derived from the expansion of the gradient in the following expression thanks to the product rule:

$$\frac{1}{2}\nabla\left[|\mathbf{E}|^2\rho\left(\frac{\partial\varepsilon}{\partial\rho}\right)\right] = \frac{1}{2}\nabla|\mathbf{E}|^2\left[\rho\left(\frac{\partial\varepsilon}{\partial\rho}\right)\right] + \frac{1}{2}|\mathbf{E}|^2\nabla\left[\rho\left(\frac{\partial\varepsilon}{\partial\rho}\right)\right].$$

The first term, driven by the non-uniformity of the electric field modulus $\nabla|\mathbf{E}|^2$, is called dielectrophoretic force, while the second part, concurrent with changes of permittivity independently of whether the field is uniform or not, is called electrocostriction force.

Using Clausius-Mossotti law, which expresses the relation of dielectric permittivity to density to a very good approximation for non-polar fluids, one can obtain that:

$$\rho\frac{\partial\varepsilon}{\partial\rho} \approx \frac{\varepsilon_0}{3}(\varepsilon_\mathrm{r}-1)(\varepsilon_\mathrm{r}+2),$$

where ε_0 is the constant permittivity of void, and $\varepsilon_\mathrm{r}$is the relative permittivity; it is worth pointing out that similar but more complex equations can be derived for polar fluids (according e.g. to [6]). The latter relation gives in turn:

$$\mathbf{f}_3 = \frac{\varepsilon_0}{6}(\varepsilon_\mathrm{r} - 1)(\varepsilon_\mathrm{r} + 2)\nabla|\mathbf{E}|^2$$

for the dielectrophoretic force and

$$\mathbf{f}_4 = |\mathbf{E}|^2 \frac{\varepsilon_0}{6}\nabla\left[(\varepsilon_\mathrm{r} - 1)\left(\varepsilon_\mathrm{r} + 2\right)\right] = |\mathbf{E}|^2 \frac{\varepsilon_0}{6}(2\varepsilon_\mathrm{r} + 1)\nabla\varepsilon_\mathrm{r}$$

for the electrocostriction force.

Dielectrophoretic force can be responsible of translational motion. The more permittive fluid (or some object within the fluid) endures a larger force and is lead to occupy regions where the electric field intensity is bigger. The direction of this term is independent of the actual field direction. Furthermore, the dielectrophoretic term is non negligible only within media whose relative permittivity is larger than unity, and can be considered to almost vanish, e.g., in the vapor phase (for most fluid in gaseous phase, $\varepsilon_\mathrm{r} \approx 1$). Fig. 2.4 shows the effects of dielectrophoretic force in two different electrode setups.

Electrostriction force is directed in the direction of increasing permittivity (e.g. from vapor to liquid) and normal to the interface (Fig. 2.5). As shown by its definition, $\mathbf{f}_4$ works in direct opposition to $\mathbf{f}_2$, decreasing the droplet size and disturbing the interface profile.

Relations between EHD force components

Recollecting the expression for each of the four contributions, the total EHD force expression reads:

$$\mathbf{f}_{\mathrm{EHD}} = \underbrace{qN_{\mathrm{p}}\mathbf{E}}_{\mathbf{f}_1} + \underbrace{\left(-\frac{1}{2}|\mathbf{E}|^2\nabla\varepsilon\right)}_{\mathbf{f}_2} + \underbrace{\frac{\varepsilon_0}{6}(\varepsilon_{\mathrm{r}}-1)(\varepsilon_{\mathrm{r}}+2)\nabla E^2}_{\mathbf{f}_3} + \underbrace{|\mathbf{E}|^2\frac{\varepsilon_0}{6}(2\varepsilon_{\mathrm{r}}+1)\nabla\varepsilon_{\mathrm{r}}}_{\mathbf{f}_4}\,. \tag{2.3}$$

Each term in (2.3) may be significant or negligible, depending on the different flow regime. The main discriminant factor is the presence or absence of a second fluid phase, while a second important feature is the relative permittivity of the fluid.

Since for the object of our study the flow is monophase, we can neglect the strong interface actions of terms $\mathbf{f}_2$ and $\mathbf{f}_4$. Moreover, since we do not want to consider large temperature gradients, the distributed effect due to ε gradient is also negligible.

As for the remaining components, we consider $\mathbf{f}_1$ to be dominant with respect to $\mathbf{f}_3$.

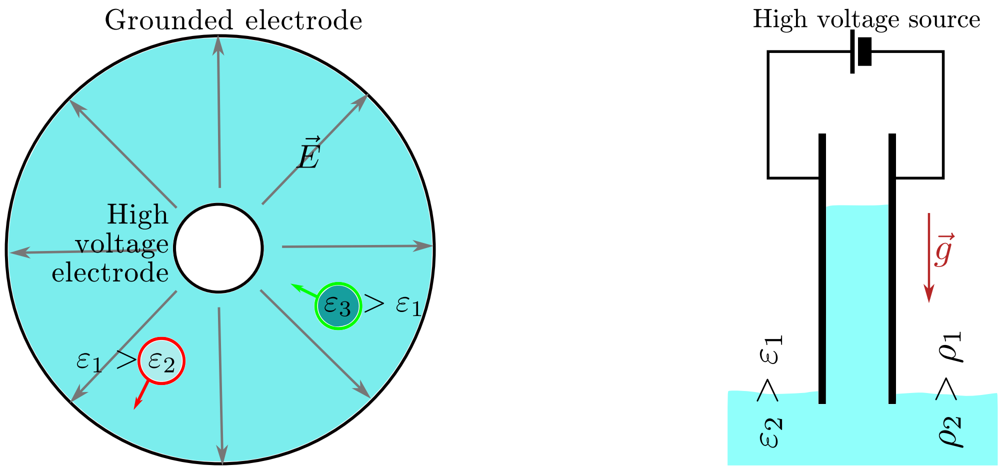

Figure 2.4: Effect of $\mathbf{f}_3$ in an capacitive systems as shown in [40]. The left picture shows two concentric cylindrical electrodes with nonuniform electric field exerting dielectrophoretic force on dielectric particles. The right picture demonstrates the same force's effect on dielectric liquid.

This latter term contains in fact the factor $\varepsilon_{\mathrm{r}} - 1$, which almost vanishes as we consider air flow ($\varepsilon_{\mathrm{r,air}} \approx 1$). Thus, from here on, we will consider

$$\mathbf{f}_{\mathrm{EHD}} = \mathbf{f}_1 = qN_{\mathrm{p}}\mathbf{E}. \tag{2.4}$$

2.2 PDE modeling of electrical discharge and fluid flow

In this section, we review the partial differential equations that govern the EHD flow, and in particular the flow of charged ions, the dependence of electric potential on charge distribution, the motion of the bulk neutral fluid and the heat transfer. Nonlinearities and couplings in the aforementioned system make its solution complicated, but some simplifications, summarized in the chart in Fig. 2.6, can be made for computational purpose.

Transport of free charge qN_{p} is governed by two fundamental equations. The first one is Poisson's equation that defines the relation between electric field (or potential) and free charge:

$$\nabla \cdot (\varepsilon\mathbf{E}) = -\nabla \cdot (\varepsilon\nabla\phi) = qN_{\mathrm{p}}. \tag{2.5}$$

The second equation is the current continuity equation, which expresses the principle of

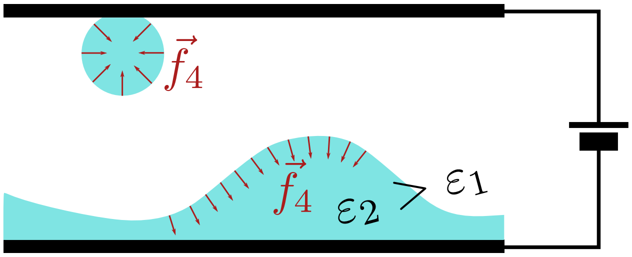

Figure 2.5: Examples of the effects of $\mathbf{f}_4$: phase interface disturbance and droplet formation (see [40, 75]).

conservation of electrical charge:

$$\frac{\partial q N_{\mathrm{p}}}{\partial t} + \nabla \cdot \mathbf{j} = 0. \tag{2.6}$$

Ion transport occurs by three different mechanisms: advection due to applied electric field, advection due to the fluid flow, and diffusion of charged particles (see e.g. [9, 10]):

$$\mathbf{j} = q N_{\mathrm{p}} \mu \mathbf{E} + q N_{\mathrm{p}} \mathbf{v} - D q \nabla N_{\mathrm{p}}. \tag{2.7}$$

The product of charge density qN_{p} and ion mobility μ is the better known electrical conductivity σ, which is normally employed in the description of solid conductors, where N_{p} can be considered constant (this lead sometimes to mix-ups like in [24] where both conductivity and mobility term sum up in the current density expression). The latter equation introduces a strong coupling between (2.5) and (2.6):

$$\frac{\partial q N_{\mathrm{p}}}{\partial t} + \nabla \cdot \big((\mu \mathbf{E} + \mathbf{v}) q \nabla N_{\mathrm{p}} - D q \nabla N_{\mathrm{p}} \big) = 0. \tag{2.8}$$

The transport field $\mathbf{v}$ in (2.8) is the bulk fluid velocity, which for a Newtonian fluid obeys the Navier-Stokes equations, which state the conservation of mass density ρ , momentum density $\rho\mathbf{v}$ and energy density $\rho C_V T$, expressed as function of fluid temperature T:

$$\frac{\partial \rho}{\partial t} + \nabla \cdot (\rho \mathbf{v}) = 0, \tag{2.9a}$$

$$\frac{\partial \rho \mathbf{v}}{\partial t} + \mathbf{v} \cdot \nabla (\rho \mathbf{v}) = \nabla \cdot (\eta \nabla \mathbf{v}) - \nabla p + \mathbf{f}_{\mathrm{vol}}, \tag{2.9b}$$

$$\frac{\partial \rho C_V T}{\partial t} + \nabla \cdot (\mathbf{v} \rho C_V T) = \nabla \cdot (k \nabla T) + Q_c + \mathbf{j} \cdot \mathbf{E} - \mathbf{v} \cdot \mathbf{f}_{\mathrm{EHD}}, \tag{2.9c}$$

where $\mathbf{g}$ is gravity acceleration, $\mathbf{f}_{\mathrm{vol}} = \mathbf{f}_{\mathrm{EHD}} + \rho \mathbf{g}$ is the body force exerted per unit volume of fluid by both gravity and the electric field, η is dynamic viscosity and k is thermal diffusion rate of the fluid. Under the assumption that the fluid is incompressible ($\frac{\partial \rho}{\partial t} = 0$) and its density and viscosity can be considered uniform ($\nabla \rho = \nabla \eta = \mathbf{0}$), (2.9a) and (2.9b) can be decoupled from (2.9c), defining the incompressible Navier-Stokes system:

$$\nabla \cdot \mathbf{v} = 0, \tag{2.10a}$$

$$\frac{\partial \mathbf{v}}{\partial t} + (\mathbf{v} \cdot \nabla)\mathbf{v} = \nu \Delta \mathbf{v} - \nabla \widetilde{p} + \frac{\mathbf{f}_{\mathrm{EHD}} + \mathbf{f}_{\mathrm{b}}}{\rho}, \tag{2.10b}$$

where ν is the kinematic viscosity,$\mathbf{f}_{\mathrm{b}}$ is an approximation for buoyancy force, and $\widetilde{p} = \left(\frac{p}{\rho} + \mathbf{g} \cdot \mathbf{x}\right)$ is a modified pressure including the hydrostatic component (we will always use $\widetilde{p}$ in the remainder, but dropping the tilde for a plain notation).

This approximation can be obtain, for small temperature gradients, by Boussinesq formula: this considers the small density variation (due to small temperature non-uniformities) to be linear with temperature differences, namely:

$$\rho(T) = \rho(T_{\mathrm{ref}})\big(1 + \beta_{\mathrm{exp}}(T_{\mathrm{ref}})(T - T_{\mathrm{ref}})\big), \tag{2.11}$$

where β_{exp} is the volumetric thermal expansivity $\frac{\mathrm{d}(-\ln \rho)}{\mathrm{d}T}|_{p=\mathrm{const.}}$ for the gas at a given temperature T_{ref} (a good approximation for T, and usually taken as a constant). For ideal gases $\beta_{\mathrm{exp}}(T) = T^{-1}$ and therefore the need for small variation for T is evident. In reasonable ranges of temperature and at ambient pressure, air can also be considered ideal gas and therefore the approximation still holds for small temperature differences. The buoyancy force term then becomes:

$$\mathbf{f}_{\mathrm{b}} = \mathbf{g}(\rho(T) - \rho(T_{\mathrm{ref}})) = \mathbf{g}\left(\rho(T_{\mathrm{ref}})\beta_{\mathrm{exp}}(T_{\mathrm{ref}})(T - T_{\mathrm{ref}})\right). \tag{2.12}$$

Going back to the energy conservation equation (2.9c)

$$\frac{\partial \rho C_V T}{\partial t} + \nabla \cdot (\mathbf{v} \rho C_V T) = \nabla \cdot (k \nabla T) + Q_c + \mathbf{j} \cdot \mathbf{E} - \mathbf{v} \cdot \mathbf{f}_{\mathrm{EHD}},$$

Q_c is the heat generation term due to e.g. chemical reactions, and can be neglected in the case of ionization, which has a small thermal output; $\mathbf{j} \cdot \mathbf{E}$ would be the Joule heating in a solid conductive material where no mechanical work is performed because of the still medium, therefore the need of subtracting the mechanical work made by the EHD force $\mathbf{v} \cdot q N_{\mathrm{p}} \mathbf{E}$. Other heating sources are external and therefore modeled as heat transfer through the boundaries. With these simplifications, and considering gas properties uniform, we can re-write the equation for temperature as:

$$\frac{\partial T}{\partial t} + \mathbf{v} \cdot \nabla T - \frac{k}{\rho C_V} \Delta T = \frac{(\mu \mathbf{E} q N_{\mathrm{p}} - D q \nabla N_{\mathrm{p}})}{\rho C_V} \cdot \mathbf{E}. \tag{2.13}$$

Equations (2.5),(2.6),(2.10) and (2.13) should be completed with suitable initial and boundary conditions, which will be clarified in Sections 2.3 and 2.4

2.3 Modeling of electron avalanche and ionization

As previously stated, in corona discharge processes, generation of free charge carriers occurs in a thin plasma layer near one electrode. In our macroscopic model, this layer is “lumped”and treated as a two-dimensional surface, so that its effect on the system is accounted for via *ad-hoc* boundary condition, completing the system of equations presented in Section 2.2. This section is split in two parts: in the first, we introduce a model for the avalanche generation of ions, which applies within the plasma layer, while in the second we propose a set of different approaches to derive the lumped BC which should reproduce the described phenomena.

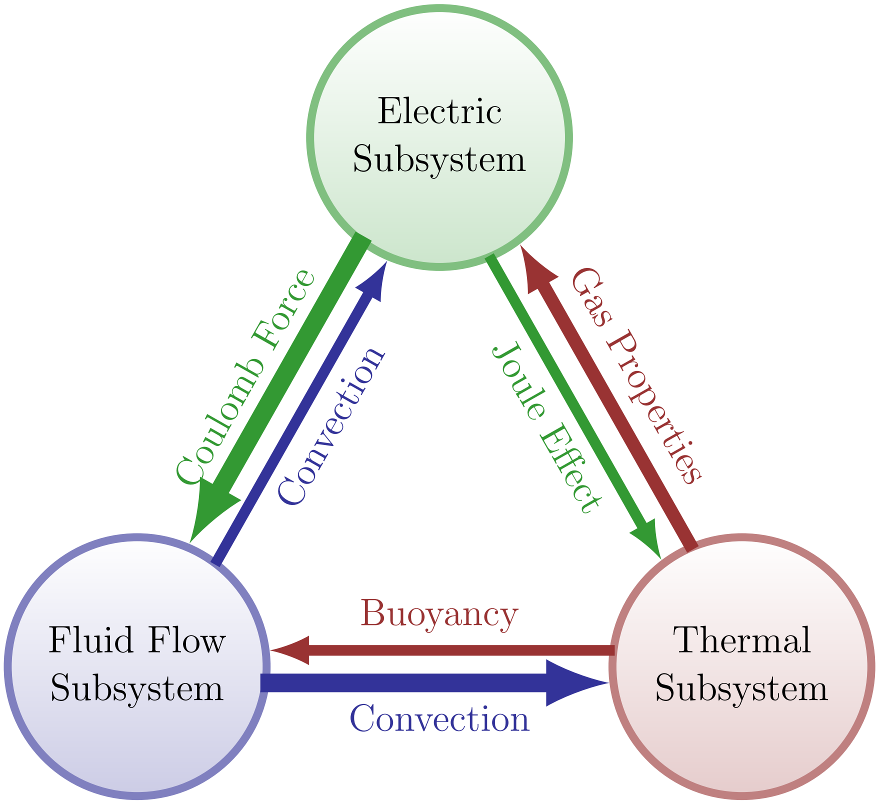

Figure 2.6: Relations between the unknowns of the EHD system, with arrows pointing to an influenced subsystems from the influencing one. Thicker arrows indicate influence which is major in most cases, while thinner ones indicate minor influence. The chart is adapted from [74].

2.3.1 Microscopic model for avalanche charge generation

The microscopic model for corona discharge relies on the model first proposed in its very core by Townsend [71, 72] and subsequently improved [70, 69], which describes the process of ionization of neutral molecules by electron impact.

Let us imagine a free electron traveling under the influence of a uniform electric field $\mathbf{E}$ (e.g. between the parallel plates of a gas filled capacitor) with mean free path $\lambda(p)$ between two collisions. If the energy that the electron gains becomes high enough, it can not only excite the hit molecule, but even detach another electron from its shell. We can define a coefficient α_{T} with the following meaning: one free electron in a gas of neutral atoms will produce by collision an average of $\mathrm{d}n = \alpha_{\mathrm{T}}\mathrm{d}x$ new electrons while traveling a path of length $\mathrm{d}x$. By solving the ODE for the total number of electrons n one obtains:

$$n(x) = n_0 \mathrm{e}^{\int_0^x \alpha_{\mathrm{T}}(s)\mathrm{d}s},$$

n_0 being the initial number of electrons emitted, e.g., by photoelectric effect at the cathode. It can be shown that α_{T} depends only on $\mathbf{E}$ and p (or $\lambda(p)$) so, in this particular case, it can be considered constant and the simpler form $n(x) = n_0\mathrm{e}^{\alpha_{\mathrm{T}} x}$ holds. Rather than a relation of the form $\alpha_{\mathrm{T}} = f(|\mathbf{E}|, p)$), the simpler form $\frac{\alpha_{\mathrm{T}}}{p} = f\left(\frac{|\mathbf{E}|}{p}\right)$ is usually employed, as the latter fits experimental data for low $\frac{|\mathbf{E}|}{p}$ range:

$$\frac{\alpha_{\mathrm{T}}}{p} = A\mathrm{e}^{B\frac{|\mathbf{E}|}{p}},$$

A, B being constants depending on the gas used. However, this relation definitely fails to hold as the $\frac{|\mathbf{E}|}{p}$ value grows over a certain threshold, and therefore other mechanisms must be accounted for. Two main phenomena can be considered in this sense, both involving a secondary electron emission: positive ion collisions with the cathode or photoelectric release due to photons coming from metastable gas atoms (excited because of the electron current itself).

Both those phenomena (and other similar ones) can be modeled with an added parameter γ_{T} usually called second Townsend coefficient, representing the average number of electrons released at the cathode for every ionizing collision happening in the gas. If we call n_1 the number of electrons released from the cathode, we will find out that n_0 were produced in the same way as in the former description (e.g. photoelectric effect *from an external photon source*) while $n_1 - n_0$ come from this secondary effect. If a total of n

electrons reach the anode, then $n - n_1$ of them have been detached from neutrals in the gas, so that the secondary contribution to the total emission becomes

$$n_1 - n_0 = \gamma_{\mathrm{T}}(n - n_1)$$

according to the definition of γ_{T} . This leads to a total electron number emitted from cathode given by

$$n_1 = \frac{n_0 + \gamma_{\mathrm{T}} n}{1 + \gamma_{\mathrm{T}}}$$

and thus to total electrons number at the anode of:

$$n = n_1 \mathrm{e}^{\alpha_{\mathrm{T}} x} = \frac{n_0 + \gamma_{\mathrm{T}} n}{1 + \gamma_{\mathrm{T}}} \mathrm{e}^{\alpha_{\mathrm{T}} x} = \cdots = n_0 \frac{\mathrm{e}^{\alpha_{\mathrm{T}} x}}{1 - \gamma_{\mathrm{T}}(\mathrm{e}^{\alpha_{\mathrm{T}} x} - 1)}, \tag{2.14}$$

x being the distance between anode and cathode plates. [1]

Again, this regime does not hold indefinitely, as at a certain point the free charge in the gas starts playing an active and non negligible role in making the electric field variable. As shown in the beginning of this section, the exponential terms in (2.14) would in that case turn into something like $\mathrm{e}^{\int_0^x \alpha_{\mathrm{T}}(s)\mathrm{d}s}$ (this does not change when the γ_{T} model is applied)

---

[1] Some prefer to use a different parameter β_{T} such that

$$\gamma_{\mathrm{T}} = \frac{\beta_{\mathrm{T}}}{\alpha_{\mathrm{T}} - \beta_{\mathrm{T}}}$$

so that the former relation becomes

$$n = n_0 \frac{(\alpha_{\mathrm{T}} - \beta_{\mathrm{T}})\mathrm{e}^{\alpha_{\mathrm{T}} x}}{\alpha_{\mathrm{T}} - \beta_{\mathrm{T}} \mathrm{e}^{\alpha_{\mathrm{T}} x}},$$

which comes in a form indeed very similar to the first formulation by Townsend. In [70], he postulated the possibility of ionization by positive ion collision (which was logical inasmuch the primary discharge was attributed to negative ions instead of electrons). Later, when a better understanding of atomic physics was achieved, this idea was proved to be wrong, being positive ions not able to detach electrons by collisions at the very small energies at which the secondary discharge was observed.

but with the further complication that now the relation becomes implicit as:

$$\frac{\alpha_{\mathrm{T}}(s)}{p} = f\left(\frac{|\mathbf{E}(n)|}{p}\right).$$

The straight Townsend discharge model becomes thus not directly applicable with relatively high currents or ion densities in the gas, but still it can turn out useful when one has to decide whether the corona discharge is triggered or not. One can indeed claim that the onset of a stable (or self-sustained) corona happens when an initial electron is able to produce enough ions to have another electron detached from the cathode. This condition translates by means of the model just provided to:

$$\gamma_{\mathrm{T}} \mathrm{e}^{\int_0^x \alpha_{\mathrm{T}}(s)\mathrm{d}s} \geqslant 1. \tag{2.15}$$

By knowledge of the monotonically increasing functional dependence of α_{T} on $\mathbf{E}$ one could then define a field intensity E_{on} depending only on p and γ_{T} that, once reached, triggers a self-sustaining discharge. At the same time a voltage V_{on} can be defined as the imposed voltage necessary to reach E_{on}. If the imposed voltage should increase over V_{on}, then the increment of space charge would initially result in a shielding of the electric field, sufficient for maintaining the discharge stable, and for further increasing in voltage, the shielding effect would not be sufficient and a disruption would happen.

The idea of a counter-effect required to maintain of a stable and self-sustaining corona discharge is what lies behind the condition called *Kaptsov hypothesis* (see [41]): the electric field value at the anode remains constant at E_{on} when a self-sustaining corona discharge is triggered, even for imposed voltage greater than V_{on}. This hypothesis is widely accepted and provides a good starting point for corona modeling.

A more precise definition for the value of E_{on} which triggers the corona may be more difficult to obtain than one could expect. For the rather simple geometry of a cylindrical pipe as cathode and a wire running trough its axis as anode, a semi-empirical solution is given, known as *Peek law* or *formula* (see [58]):

$$E_{\mathrm{on}} = E_0 C_1 \frac{p}{p_0} \left(1 + \sqrt{\frac{p_0 C_2}{p r_{\mathrm{w}}}} \right), \tag{2.16}$$

where E_0 is the arc breakdown field at atmospheric pressure p_0, r_{w} is the wire radius, C_1 a factor depending on the material and roughness of electrodes, and C_2 a constant length (discriminating between small and big radii).

2.3.2 Boundary lumped models for corona discharge

With the counter-effect behavior described in the latest subsection in mind, we propose in this section four different boundary conditions formulations to be imposed together with equation (2.6), in order to effectively reproduce corona discharge.

The boundary conditions will be presented in the form of a Robin condition, namely:

$$\alpha N_{\mathrm{p}} + \beta \partial_{\mathbf{n}} N_{\mathrm{p}} = \kappa, \tag{2.17}$$

where α , β and κ can in general depend on E_n , the electric field normal to the electrode surface, while $\partial_{\mathbf{n}} N_{\mathrm{p}} = \mathbf{n} \cdot \nabla N_{\mathrm{p}}$ is the gradient component normal to the boundary surface.

The first approach consists in imposing an experimentally measured current i_{m} trough a uniform current density normal to the surface j_n . In order for the total current to match the experimental value, the current density must be given by the ratio between i_{m} and the electrode surface area s. Thanks to (2.7), we have:

$$\underbrace{\mu E_n q}_{\alpha} N_{\mathrm{p}} + \underbrace{Dq}_{\beta} \partial_{\mathbf{n}} N_{\mathrm{p}} = \underbrace{\tfrac{i_{\mathrm{m}}}{s}}_{\kappa}. \tag{2.18}$$

This approach, at least in its principle of matching empirical currents, has been adopted by several authors (e.g. in [35, 51, 52, 76]). Nonetheless, it has flaws in two different aspects: it is a non-predictive condition, since it needs experimental data which are not always available, and it fails to produce higher current density where E_n is higher, which is one of the desirable properties according to the microscopic model presented in this same section.

To provide a model in which j_n monotonically increases in relation with E_n, several possibilities are available. The second model we present, called "space charge controlled current" (SCCC), is proposed e.g. in [15], and contains two of the properties already described here: a threshold on the electric field which reproduces the effect described by (2.15), and the shielding effect of free charge. The law describing the injection reads then

$$j_n = j_{\mathrm{sat}} H(E_n - E_{\mathrm{on}}) - w N_{\mathrm{p}}, \tag{2.19}$$

where j_{sat} is the maximum current density the contact is supposed to allow, H is the step function valued 0 for negative arguments and 1 for nonnegative ones, E_{on} is the threshold field given by (2.16), and w is a quantity with the dimensions of a velocity times an electric charge, which originates a *backscattering* current that grows as the free carriers density rises. Transformed to our standard formulation (2.17), it reads:

$$\underbrace{\mu E_n q + w}_{\alpha} N_{\mathrm{p}} + \underbrace{Dq}_{\beta} \partial_{\mathbf{n}} N_{\mathrm{p}} = \underbrace{j_{\mathrm{sat}} H(E_n - E_{\mathrm{on}})}_{\kappa}. \tag{2.20}$$

This formulation solves the two flaws which we evidenced in (2.18), since it is predictive and, to a certain extent, allows for higher currents as E_n grows. The choice of the parameters j_{sat} and w is nonetheless critical: the assumptions in the model root require in fact the saturation and backscattering current densities j_{sat} and wN_{p} to be much bigger than the actual value of j_n , in order for current to be “space charge controlled”, while when j_n is big the control over the current is mainly exerted by the j_{sat} parameter.

A third option is to directly enforce Kaptsov hypothesis of a constant electric field where ions are produced. This ansatz has been adopted, even if with different methods for its actual enforcement, by different authors (e.g. in [1, 39, 42]). Our implementation is obtained by imposing that the ion density and electric field at the electrode verify the implicit relation

$$N_{\mathrm{p}}(E_n - E_{\mathrm{on}}) = 0, \tag{2.21}$$

which allows only one of the factors to be nonzero at the same time; it recalls the form of the characteristic equation of an ideal diode, where any current is allowed, but only over a threshold voltage. The implicit relation cannot be effectively represented in the usual form (2.17) without allowing the coefficients, and in particular κ , to depend on N_{p} itself (being α and β valued 1 and 0 respectively):

$$N_{\mathrm{p}} = \underbrace{N_{\mathrm{p}}\frac{E_n}{E_{\mathrm{on}}}}_{\kappa}\,. \tag{2.22}$$

This choice allows for a formulation suitable for iterative solution algorithms, allowing the free charge value to grow in order to enhance the shielding effect in cases where the electric field is rather high, while cutting it to lower values if the shield effect brings E_n under the defined threshold E_{on}. This latter parameter has the advantage of being easy to measure or determine, and a rather good estimate can be given in most cases by Peek’s law (2.16). Nonetheless, the non-smooth relation originating this “ideal diode” boundary condition makes it rather unstable, and not easy to apply numerically.

The fourth and last form of boundary condition considered in this work is presented here for the first time and may be seen as a generalization, or a smoother version, of the

Table 2.1: Summary of the coefficients for the four boundary models presented

Model name	Equation	α	β	κ
Uniform	2.18	$q\mu E_n$	qD	$\dfrac{i_{\mathrm{exp}}}{s}$
SCCC	2.20	$q\mu E_n + w$	qD	$j_{\mathrm{sat}} H\left(E_n - E_{\mathrm{on}}\right)$
Ideal diode	2.22	1	0	$N_{\mathrm{p}} \dfrac{E_n}{E_{\mathrm{on}}}$
Real diode	2.23	1	0	$\widetilde{N_{\mathrm{p}}} \exp\left(\dfrac{E_n}{E_{\mathrm{ref}}}\right)$

"ideal diode" condition (2.22), expressed in form of exponential growth in ion density with growing electric field. We will refer to this model as "real diode":

$$N_{\mathrm{p}} = \underbrace{\widetilde{N_{\mathrm{p}}} \exp\left(\frac{E_n}{E_{\mathrm{ref}}}\right)}_{\kappa}. \tag{2.23}$$

It is easy to see that the set of points in the N_{p}-E_n plane that verify (2.23) converges to the set verifying (2.21), as $E_{\mathrm{ref}} \to 0$ and at the same time $\widetilde{N_{\mathrm{p}}} \to \exp\left(\frac{-E_{\mathrm{on}}}{E_{\mathrm{ref}}}\right)$. The advantages the "real diode" formulation provides rely on its smoothness, which makes its numerical implementation much easier, and on the presence of two parameters, allowing for more flexibility when trying to fit experimental data. The drawbacks of this approach resides also in the parameters, which cannot be easily connected to any experimentally measurable value as, e.g., E_{on} is.

A summary of the coefficients is presented in Table 2.1 while a comparison, in terms of N_{p}-E_n characteristic curve, is given in Fig. 2.7. Neglecting the gradient term in the BC, at least for representation purposes, makes sense since drift current is expected to outweigh diffusion current in the anode region, where the electric field assumes very high values.

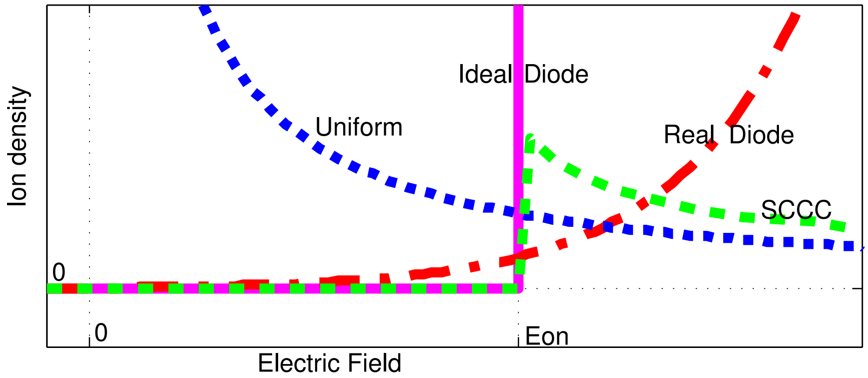

Figure 2.7: Representation of the four different boundary models in the N_p-E_n plane

2.4 Summary of the PDE system and boundary conditions

The equations presented in sec. 2.2 are complemented with proper boundary and initial conditions. Figure 2.8 shows a simple two-dimensional space domain Ω, whose boundary $\partial\Omega$ is partitioned in five different subsets:

- Γ_A represents the anode, thus a positive voltage and an ion density (whose dependence on the electric field will be discussed in next chapter) will be imposed;
- Γ_C represents the cathode, thus zero voltage and no diffusion current are imposed;
- Γ_I represents an electrically insulating wall, thus zero electric field and zero diffusion current are imposed. These first three boundary types are all treated as solid walls for the fluid and thermal equations, thus zero velocity (no-slip condition), and fixed incoming energy are imposed;
- Γ_in represents a fluid inlet, thus the values of all velocity components and of temperature are imposed, while all the other variable are considered to have no sensible gradients;
- Γ_out represents a fluid outlet, thus the internal stress of the fluid is usually considered

to vanish, as all other gradients are.

Additionally, the initial values for the unknowns are supposed to be consistent with the boundary conditions, and the initial velocity field $\mathbf{v}_0$ to be divergence free. Summarizing, the whole model is given by the following equations:

Poisson equation

$$\begin{cases} -\nabla \cdot (\varepsilon \nabla \phi) = q N_{\mathrm{p}} & \text{on } \Omega \times (0, \bar{t}) \\ \phi = V_{\mathrm{A}} & \text{on } \Gamma_{\mathrm{A}} \times (0, \bar{t}) \\ \phi = 0 & \text{on } \Gamma_{\mathrm{C}} \times (0, \bar{t}) \\ \partial_{\mathbf{n}} \phi = 0 & \text{on } (\Gamma_{\mathrm{I}} \cup \Gamma_{\mathrm{in}} \cup \Gamma_{\mathrm{out}}) \times (0, \bar{t}) \end{cases} \tag{2.24a}$$

Charge conservation equation

$$\begin{cases} \dfrac{\partial (q N_{\mathrm{p}})}{\partial t} + \nabla \cdot (-D q \nabla N_{\mathrm{p}} + (\mathbf{v} + \mu \mathbf{E}) q N_{\mathrm{p}}) = 0 & \text{on } \Omega \times (0, \bar{t}) \\ \alpha N_{\mathrm{p}} + \beta \partial_{\mathbf{n}} N_{\mathrm{p}} = \kappa & \text{on } \Gamma_{\mathrm{A}} \times (0, \bar{t}) \\ \partial_{\mathbf{n}} N_{\mathrm{p}} = 0 & \text{on } (\partial\Omega \backslash \overline{\Gamma_{\mathrm{A}}}) \times (0, \bar{t}) \\ N_{\mathrm{p}} = N_{\mathrm{p}0} & \text{on } \Omega \text{ for } t = 0 \end{cases} \tag{2.24b}$$

Navier-Stokes equations

$$\begin{cases} \dfrac{\partial \mathbf{v}}{\partial t} - \nabla \cdot (\nu \nabla \mathbf{v}) + (\mathbf{v} \cdot \nabla) \mathbf{v} - \nabla p = \dfrac{\mathbf{f}_{\mathrm{EHD}} + \mathbf{f}_{\mathrm{b}}}{\rho} & \text{on } \Omega \times (0, \bar{t}) \\ \nabla \cdot \mathbf{v} = 0 & \text{on } \Omega \times (0, \bar{t}) \\ \mathbf{v} = 0 & \text{on } (\Gamma_{\mathrm{A}} \cup \Gamma_{\mathrm{C}} \cup \Gamma_{\mathrm{I}}) \times (0, \bar{t}) \\ \mathbf{v} = \mathbf{v}_{\mathrm{in}} & \text{on } \Gamma_{\mathrm{in}} \times (0, \bar{t}) \\ -\nu \partial_{\mathbf{n}} \mathbf{v} + p \mathbf{n} = 0 & \text{on } \Gamma_{\mathrm{out}} \times (0, \bar{t}) \\ \mathbf{v} = \mathbf{v}_0 & \text{on } \Omega \text{ for } t = 0 \end{cases} \tag{2.24c}$$

Temperature equation

$$\begin{cases} \dfrac{\partial(\rho C_V T)}{\partial t} + \nabla\cdot(-k\nabla T + \mathbf{v}\rho C_V T) = (\mu \mathbf{E} q N_\mathrm{p} - D q \nabla N_\mathrm{p})\cdot\mathbf{E} & \text{on } \Omega\times(0,\bar{t}) \\ k\partial_\mathbf{n} T = e_\mathrm{in} & \text{on } (\Gamma_\mathrm{A}\cup\Gamma_\mathrm{C}\cup\Gamma_\mathrm{I})\times(0,\bar{t}) \\ T = T_\mathrm{in} & \text{on } \Gamma_\mathrm{in}\times(0,\bar{t}) \\ k\partial_\mathbf{n} T = 0 & \text{on } \Gamma_\mathrm{out}\times(0,\bar{t}) \\ T = T_0 & \text{on } \Omega \text{ for } t=0 \end{cases} \tag{2.24d}$$

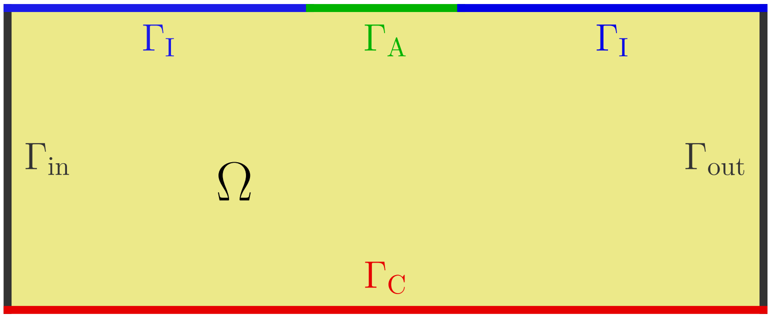

Figure 2.8: Example domain where all the five possible kind of boundary are depicted.

Chapter 3

Numerical solution of the Electrohydrodynamics equations

A solution for the problem introduced in section 2.4 is known in analytic form only in very simple cases, and numerical approximation has to be employed. This chapter is devoted to explaining how a suitable algorithm to deal with the problem's different nonlinearities and couplings has been obtained, and is structured as follows: in Section 3.1 time discretization and formulation of a semi-discrete problem are addressed, in Section 3.2 we deal with the decoupling of the electrical, fluid and thermal subsystems, in Section 3.3 the electric subproblem is decoupled and linearized, in Section 3.4 we introduce the finite volume space discretization for the general diffusion-advection-reaction equation, and in the end in Section 3.5 split operators solution algorithm for the fluid variables is presented.

3.1 Semi-discrete problem formulation

In this section, we provide the formulation of an initial/boundary value problem defined by the equations presented in Ch. 2, and then we introduce the semi-discrete formulation for advancing in time. For this purpose, it is useful to see the unknowns as functions defined on the time interval $[0, \bar{t}]$ into suitably chosen functional spaces.

More precisely, let $\Omega \subset \mathbb{R}^3$ be the spatial domain, with boundary $\partial\Omega$ sufficiently regular for the trace and Green's formulas to hold. The solution of the continuous problem will be denoted by:

$$\mathbf{u} : [0, \bar{t}] \mapsto \mathbb{U} \subset \widehat{\mathbb{U}} \tag{3.1}$$

where $\mathbf{u} = [\phi, N_{\mathrm{p}}, \mathbf{v}, p, T]$, $\widehat{\mathbb{U}}$ is the functional space

$$\widehat{\mathbb{U}} = \underbrace{H^1(\Omega)}_{\phi} \times \underbrace{H^1(\Omega)}_{N_{\mathrm{p}}} \times \left(\underbrace{H^1(\Omega) \times H^1(\Omega) \times H^1(\Omega)}_{\mathbf{v}} \right) \times \underbrace{L^2(\Omega)}_{p} \times \underbrace{H^1(\Omega)}_{T} \tag{3.2}$$

and $\mathbb{U}$ is the subset of $\widehat{\mathbb{U}}$ enforcing the imposed boundary conditions. With this notation, we can readily re-write the problem as a nonlinear initial value one, namely finding $\mathbf{u}$ such that:

$$\begin{cases} F(t, \mathbf{u}(t), \frac{\partial \mathbf{u}}{\partial t}(t)) = 0 \quad \forall t \in (0, \bar{t}) \\ \mathbf{u}(0) = \mathbf{u}_0. \end{cases} \tag{3.3}$$

The classical solution of the reformulated problem will then be found in $C^1([0, \bar{t}]; \mathbb{U})$. A time semi-discrete problem is then obtained by substituting time derivatives in (3.3) with suitable difference formulas.

Let the discrete time domain be formed by a set of time instants $t^{(i)} = i\delta t$ with $0 < \delta t \in \mathbb{R}$ and i a non negative integer index. Let also $\mathbf{u}^{(i)}$ denote the value of the solution at the instant $t^{(i)} = i\delta t$. The time derivatives will then be substituted by combinations of the solution values at different times; for example, if we decide to employ the classical backward Euler approximation:

$$\left. \frac{\partial \mathbf{u}}{\partial t} \right|_{t^{(i)}} \approx \frac{\mathbf{u}^{(i)} - \mathbf{u}^{(i-1)}}{\delta t}, \tag{3.4}$$

then the problem in (3.3), properly restricted on the discrete time domain, becomes

$$\begin{cases} G(\mathbf{u}^{(i)}; i, \mathbf{u}^{(i-1)}, \delta t) = F(i\delta t, \mathbf{u}^{(i)}, \frac{\mathbf{u}^{(i)} - \mathbf{u}^{(i-1)}}{\delta t}) = 0 \quad \forall i : i\delta t \in (0, \bar{t}) \\ \mathbf{u}^0 = \mathbf{u}_0 \end{cases}, \tag{3.5}$$

which is a discrete dynamical system in $\mathbb{U}$ where the time advancing map is implicitly represented by (3.5); in Sec. 3.2, a detailed presentation of a suitable algorithm for its solution,in terms of fixed point iterations, is presented. For sake of convenience, we report explicitly the stationary problem to be solved at the i-th step in problem (3.5), dropping the step index for quantities evaluated at the i-th step and substituting the superscript $^{(i-1)}$ with $^{\text{old}}$:

Poisson equation

$$\begin{cases} -\nabla \cdot (\varepsilon \nabla \phi) = q N_{\text{p}} & \text{on } \Omega \\ \phi = V_{\text{A}} & \text{on } \Gamma_{\text{A}} \\ \phi = 0 & \text{on } \Gamma_{\text{C}} \\ \partial_{\mathbf{n}} \phi = 0 & \text{on } \Gamma_{\text{I}} \cup \Gamma_{\text{in}} \cup \Gamma_{\text{out}} \end{cases} \tag{3.6a}$$

Charge conservation (backward Euler)

$$\begin{cases} \dfrac{q(N_{\text{p}} - N_{\text{p}}^{\text{old}})}{\delta t} + \nabla \cdot (-Dq\nabla N_{\text{p}} + (\mathbf{v} - \mu \nabla \phi) q N_{\text{p}}) = 0 & \text{on } \Omega \\ \alpha N_{\text{p}} + \beta \partial_{\mathbf{n}} N_{\text{p}} = \kappa & \text{on } \Gamma_{\text{A}} \\ \partial_{\mathbf{n}} N_{\text{p}} = 0 & \text{on } (\partial\Omega \backslash \overline{\Gamma_{\text{A}}}) \end{cases} \tag{3.6b}$$

Navier-Stokes equations (backward Euler)

$$\begin{cases} \dfrac{\mathbf{v}-\mathbf{v}^{\text{old}}}{\delta t} - \nabla\cdot(\nu\nabla\mathbf{v}) + (\mathbf{v}\cdot\nabla)\mathbf{v} - \nabla p = \dfrac{\mathbf{f}_{\text{EHD}}+\mathbf{f}_{\text{b}}}{\rho} & \text{on } \Omega \\ \nabla\cdot\mathbf{v} = 0 & \text{on } \Omega \\ \mathbf{v}\cdot\mathbf{n} = 0 & \text{on } \Gamma_{\text{A}}\cup\Gamma_{\text{C}}\cup\Gamma_{\text{I}} \\ \mathbf{v} = \mathbf{v}_{\text{in}} & \text{on } \Gamma_{\text{in}} \\ -\nu\partial_{\mathbf{n}}\mathbf{v} + p\mathbf{n} = 0 & \text{on } \Gamma_{\text{out}} \end{cases} \tag{3.6c}$$

Temperature equation (backward Euler)

$$\begin{cases} \dfrac{\rho C_V(T-T^{\text{old}})}{\delta t} + \nabla\cdot(-k\nabla T + \mathbf{v}\rho C_V T) = (\mu\mathbf{E}qN_{\text{p}} - Dq\nabla N_{\text{p}})\cdot\mathbf{E} & \text{on } \Omega \\ k\partial_{\mathbf{n}}T = e_{\text{in}} & \text{on } \Gamma_{\text{A}}\cup\Gamma_{\text{C}}\cup\Gamma_{\text{I}} \\ T = T_{\text{in}} & \text{on } \Gamma_{\text{in}} \\ k\partial_{\mathbf{n}}T = 0 & \text{on } \Gamma_{\text{out}} \end{cases} \tag{3.6d}$$

In the forthcoming sections we will describe an iterative technique to solve system (3.6), based on a set of nested fixed point iterations.

3.2 Functional iteration for the solution of the semi-discrete problem

Advancing in time for the dynamical system (3.5) involves the solution of a coupled set of nonlinear PDEs of the form (3.6). The approach adopted in this work for the solution of (3.6) is based on a set of nested fixed point iterations, following closely the structure of algorithms presented in [49, 50, 32, 14, 20, 19]. The present section will introduce the maps used for the outermost level of the iteration, depicted in Figure 3.1

We characterize the solution of (3.6) as the fixed point of the map $\mathcal{M} : \mathbb{U} \mapsto \mathbb{U}$ such that for $\mathbf{w} \in \mathbb{U}$:

$$\mathbf{w} = \mathcal{M}(\mathbf{w}) \Leftrightarrow G(\mathbf{w}; i, \mathbf{u}^{\text{old}}, \delta t) = 0. \tag{3.7}$$

As it is apparent from the right hand side term of (3.7), the map depends also on values of the unknowns at the previous time step. These values should, in principle, appear as parameters in the map $\mathcal{M}$; for sake of notational clarity, though, we will drop them in the following. The staggered formulation, which paves the way for a consistent solution algorithm, can be now obtained by splitting the computation of $\mathcal{M}(\mathbf{w})$ as a composition of three maps, which work through subspaces of $\widetilde{\mathbb{U}}$:

$$\mathcal{M} = \mathcal{T} \circ \mathcal{F} \circ \mathcal{E}. \tag{3.8}$$

The definition of each one of the functional mappings $\mathcal{E}$, $\mathcal{F}$ and $\mathcal{T}$ is given below by characterizing them as the resolvent operator of one of the differential subproblems describing a specific physical aspect of the coupled system.

- $\mathcal{E}$ represents the solution map of the Poisson-drift-diffusion system (3.6a)-(3.6b) for the electrical variables, with "frozen" fluid velocity and physical properties:

$$\mathbf{w}^* = \mathcal{E}(\mathbf{w})$$

$$\Updownarrow$$

$$\begin{cases} -\nabla \cdot (\varepsilon \nabla \phi^*) = q N_{\text{p}}^* & \text{on } \Omega \\ \phi^* = V_{\text{A}} & \text{on } \Gamma_{\text{A}} \\ \phi^* = 0 & \text{on } \Gamma_{\text{C}} \\ \partial_{\mathbf{n}} \phi^* = 0 & \text{on } \Gamma_{\text{I}} \cup \Gamma_{\text{in}} \cup \Gamma_{\text{out}} \\ \frac{q(N_{\text{p}}^* - N_{\text{p}}^{\text{old}})}{\delta t} + \nabla \cdot \left(-Dq\nabla N_{\text{p}}^* + (\mathbf{v} - \mu \nabla \phi^*) q N_{\text{p}}^*\right) = 0 & \text{on } \Omega \\ \alpha(\phi^*) N_{\text{p}}^* + \beta(\phi^*) \mathbf{n} \cdot \nabla N_{\text{p}}^* = \kappa(\phi^*, N_{\text{p}}^*) & \text{on } \Gamma_{\text{A}} \\ \partial_{\mathbf{n}} N_{\text{p}}^* = 0 & \text{on } (\partial\Omega \backslash \overline{\Gamma_{\text{A}}}) \\ \mathbf{v}^* = \mathbf{v}, p^* = p, T^* = T & \text{on } \Omega \end{cases} \tag{3.9}$$

- $\mathcal{F}$ represents the solution map of the Navier-Stokes equations (3.6c) for the fluid variables, with a "frozen" source term depending on the electrical and thermal variables, and physical properties depending from temperature:

$$\mathbf{w}^* = \mathcal{F}(\mathbf{w})$$

$$\Updownarrow$$

$$\begin{cases} \frac{\mathbf{v}^* - \mathbf{v}^{\text{old}}}{\delta t} - \nabla \cdot (\nu \nabla \mathbf{v}^*) + (\mathbf{v}^* \cdot \nabla)\mathbf{v}^* - \nabla p^* = \frac{\mathbf{f}_{\text{EHD}} + \mathbf{f}_{\text{b}}}{\rho} & \text{on } \Omega \\ \nabla \cdot \mathbf{v}^* = 0 & \text{on } \Omega \\ \mathbf{v}^* \cdot \mathbf{n} = 0 & \text{on } \Gamma_{\text{A}} \cup \Gamma_{\text{C}} \cup \Gamma_{\text{I}} \\ \mathbf{v}^* = \mathbf{v}_{\text{in}} & \text{on } \Gamma_{\text{in}} \\ -\nu \partial_{\mathbf{n}} \mathbf{v}^* + p^* \mathbf{n} = 0 & \text{on } \Gamma_{\text{out}} \\ \phi^* = \phi, N_{\text{p}}^* = N_{\text{p}}, T^* = T & \text{on } \Omega \end{cases} \tag{3.10}$$

- $\mathcal{T}$ represents the solution map of the temperature equation (3.6d), with "frozen" velocity field and source term depending on the electrical variables:

$$\mathbf{w}^* = \mathcal{T}(\mathbf{w})$$

$$\Updownarrow$$

$$\begin{cases} \frac{\rho C_V (T^* - T^{\text{old}})}{\delta t} + \nabla \cdot (-k \nabla T^* + \mathbf{v} \rho C_V T^*) = (\mu \mathbf{E} q N_{\text{p}} - D q \nabla N_{\text{p}}) \cdot \mathbf{E} & \text{on } \Omega \\ k \partial_{\mathbf{n}} T^* = e_{\text{in}} & \text{on } \Gamma_{\text{A}} \cup \Gamma_{\text{C}} \cup \Gamma_{\text{I}} \\ T^* = T_{\text{in}} & \text{on } \Gamma_{\text{in}} \\ k \partial_{\mathbf{n}} T^* = 0 & \text{on } \Gamma_{\text{out}} \\ \phi^* = \phi, N_{\text{p}}^* = N_{\text{p}}, \mathbf{v}^* = \mathbf{v}, p^* = p & \text{on } \Omega \end{cases} \tag{3.11}$$

The order in which the maps are applied is also not arbitrary: in fact, as already pointed out in Fig. 2.6, it reflects the order of influence of one component to another.

The contractivity of the map $\mathcal{M}$ has been observed in the numerical simulations of Chapter 4, but has not been proved analytically. The analysis of the contractivity problems could be carried out, e.g., with the mathematical instruments introduced in [17, Ch.9], and

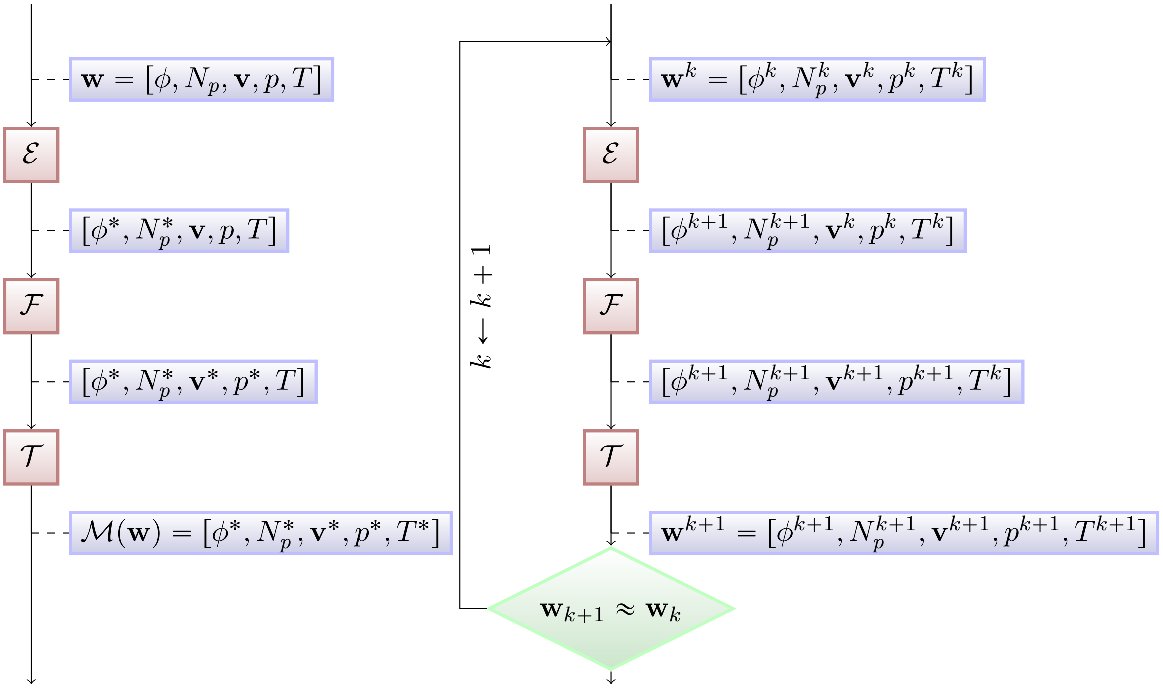

Figure 3.1: Block diagrams representing the application of $\mathcal{M}$ (left) and the iterative algorithm for fixed point search employing its application (right).

would be an extension of the work of the already cited [49, 50, 32, etc.], but it is beyond the scope of this thesis.

3.3 Functional iteration for the electric subproblem solution

The solution of the electrical subproblem, which has been represented in (3.8) with the computation of $\mathcal{E}(\mathbf{w})$ for some element $\mathbf{w} \in \mathbb{U}$, entails dealing once more with nonlinear coupling between equations (3.6a) and (3.6b). This section presents the approach employed, in a framework very similar to the global one considered in 3.2, introducing then a modified version of equation (3.6a) to enforce convergence.

Let $\widetilde{\mathbb{U}} = H^1(\Omega) \times H^1(\Omega)$ represent the restriction on the first two components of $\mathbb{U}$. We define $\mathcal{E}$ in terms of the map $\mathcal{M}_{\mathcal{E}}$, from $\widetilde{\mathbb{U}}$ onto itself, by means of the following relation:

$$\mathbf{w}^* = \mathcal{E}(\mathbf{w}) \Leftrightarrow \begin{cases} \mathcal{M}_{\mathcal{E}}([\phi^*, N_{\mathrm{p}}^*]; \mathbf{v}, p, T) = [\phi^*, N_{\mathrm{p}}^*] \\ \mathbf{v}^* = \mathbf{v}, p^* = p, T^* = T. \end{cases} \tag{3.12}$$

The map $\mathcal{M}_{\mathcal{E}}$ is given by the composition of the two maps $\mathcal{P}$ and $\mathcal{C}$, in turn defined as the solution maps for Poisson and semi-discrete charge conservation equations. More explicitly:

$$\mathcal{M}_{\mathcal{E}} = \mathcal{C} \circ \mathcal{P} \tag{3.13}$$

with

$$[\phi^*, N_{\mathrm{p}}^*] = \mathcal{P}([\phi, N_{\mathrm{p}}])$$

$$\Updownarrow$$

$$\begin{cases} -\nabla \cdot (\varepsilon \nabla \phi^*) = q N_{\mathrm{p}} & \text{on } \Omega \\ \phi^* = V_{\mathrm{A}} & \text{on } \Gamma_{\mathrm{A}}, \forall i > 0 \\ \phi^* = 0 & \text{on } \Gamma_{\mathrm{C}} \\ \partial_{\mathbf{n}} \phi^* = 0 & \text{on } \Gamma_{\mathrm{I}} \cup \Gamma_{\mathrm{in}} \cup \Gamma_{\mathrm{out}} \\ N_{\mathrm{p}}^* = N_{\mathrm{p}} & \text{on } \Omega \end{cases} \tag{3.14}$$

and

$$[\phi^*, N_\mathrm{p}^*] = \mathcal{C}([\phi, N_\mathrm{p}])$$

$$\Updownarrow$$

$$\begin{cases} \frac{q(N_\mathrm{p}^* - N_\mathrm{p}^\mathrm{old})}{\delta t} + \nabla \cdot \left(-Dq\nabla N_\mathrm{p}^* + (\mathbf{v} - \mu\nabla\phi)qN_\mathrm{p}^*\right) = 0 & \text{on } \Omega \\ \alpha(\phi)N_\mathrm{p}^* = \kappa(\phi, N_\mathrm{p}) - \beta(\phi)\partial_\mathbf{n} N_\mathrm{p} & \text{on } \Gamma_\mathrm{A} \\ \partial_\mathbf{n} N_\mathrm{p}^* = 0 & \text{on } (\partial\Omega \backslash \overline{\Gamma_\mathrm{A}}) \\ \phi^* = \phi & \text{on } \Omega. \end{cases} \tag{3.15}$$

where from $(3.15)_2$ is clear how the Robin condition (2.17) on Γ_A has been actually transformed in a Dirichlet one via the explicit treatment of the gradient term.

The same procedure as in Sect. 3.2 could be applied for finding $\mathcal{E}(\mathbf{w})$ given $\mathbf{w}$, but unfortunately the convergence of such method is not guaranteed. In place of it, a modified version obtained trough a variable change has been employed. Let $\widetilde{N_\mathrm{p}}$ be a constant number density, $\phi_\mathrm{E} = \frac{k_\mathrm{B}T}{q}$ be Einstein potential, and ζ be a potential defined by the law:

$$N_\mathrm{p} = \widetilde{N_\mathrm{p}} \exp\left(\frac{\zeta - \phi}{\phi_\mathrm{E}}\right). \tag{3.16}$$

Enforcing this relation and substituting it in (2.24a) and (2.24b), it is possible to look for a solution in terms of ζ instead of N_p.

If the same construction based on fixed point iterations is adopted, this new formulation provides a converging algorithm, at the cost of having to deal with a nonlinear version of Poisson equation. Furthermore, iterative framework allows to never actually “compute”the newly introduced potential. In fact, when solving Poisson problem, one would use the latest computed value for ζ, which can be readily expressed in terms of the latest ϕ and N_p value available. In terms of the maps previously defined, this means quite simply that $\mathcal{P}$

is substituted by its nonlinear version $\widetilde{\mathcal{P}}$:

$$[\phi^*, N_\mathrm{p}^*] = \widetilde{\mathcal{P}}([\phi, N_\mathrm{p}])$$

$$\Updownarrow$$

$$\begin{cases} -\nabla \cdot (\varepsilon \nabla \phi^*) = q N_\mathrm{p} \exp\left(\dfrac{\phi - \phi^*}{\phi_\mathrm{E}}\right) & \text{on } \Omega \\ \phi^* = V_\mathrm{A} & \text{on } \Gamma_\mathrm{A}, \forall i > 0 \\ \phi^* = 0 & \text{on } \Gamma_\mathrm{C} \\ \partial_\mathbf{n} \phi^* = 0 & \text{on } \Gamma_\mathrm{I} \cup \Gamma_\mathrm{in} \cup \Gamma_\mathrm{out} \\ N_\mathrm{p}^* = N_\mathrm{p} & \text{on } \Omega. \end{cases} \tag{3.17}$$

Notice that the two maps $\mathcal{C} \circ \mathcal{P}$ and $\mathcal{C} \circ \widetilde{\mathcal{P}}$ have the exact same fixed points, since at a fixed point the exponential term in (3.17) reduces to 1. Last step to be taken, as the equations are uncoupled and iteratively solved for, is the linearization of the new version of Poisson equation. This equation belongs to the class of quasi-linear equations, and the Newton-Raphson algorithm was chosen for its solution. Each iteration of the method (which we will see as the application of a map called $\overline{\mathcal{P}}_{\overline{\phi}}$) can be interpreted as an incremental step: computing a solution variation $\delta\phi$ under the assumption that summing it to the current solution estimation ϕ leads to the exact solution of the nonlinear problem $\phi + \delta\phi$. In formulas (deriving from (3.6a) and (3.17)):

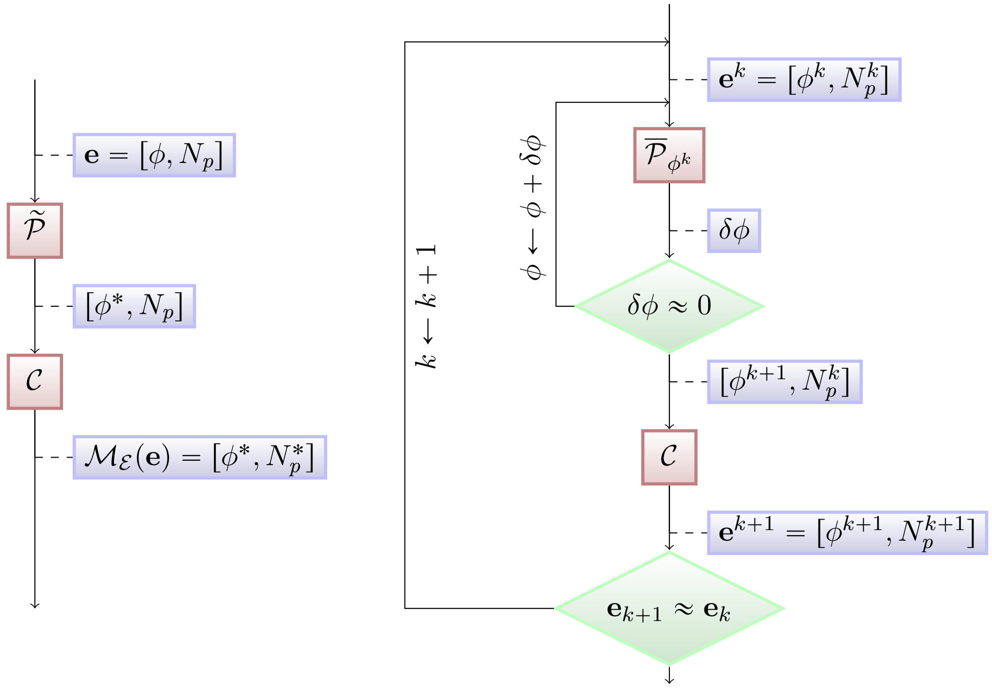

Figure 3.2: Block diagrams representing the application of $\mathcal{M}_\mathcal{E}$ (left) and the iterative algorithm for fixed point search employing both its application and Newton-Raphson iteration (right).

$$
\begin{gathered}
[\phi^*, N_\mathrm{p}^*] = \overline{\mathcal{P}}_{\overline{\phi}}([\phi, N_\mathrm{p}]) \\
\Updownarrow \\
\begin{cases}
-\nabla \cdot (\varepsilon \nabla(\phi + \delta\phi)) = q N_\mathrm{p} \left(\dfrac{\phi_\mathrm{E} - \delta\phi}{\phi_\mathrm{E}}\right) \exp\left(\dfrac{\overline{\phi} - \phi}{\phi_\mathrm{E}}\right) \cancel{\pm o(\delta\phi)} & \text{on } \Omega \\
\delta\phi = 0 & \text{on } \Gamma_\mathrm{A} \cup \Gamma_\mathrm{C} \\
\partial_\mathbf{n} \phi = 0 & \text{on } \Gamma_\mathrm{I} \cup \Gamma_\mathrm{in} \cup \Gamma_\mathrm{out} \\
N_\mathrm{p}^* = N_\mathrm{p}, \phi^* = \phi + \delta\phi & \text{on } \Omega
\end{cases}
\end{gathered}
\tag{3.18}
$$

where the subscript parameter $\overline{\phi}$ indicates the potential used as first argument in the exponential term (which is part of the ζ estimation as per (3.16), and therefore linked to

N_{p} which does not change), while the erased term ~~$+o(\delta\phi)$~~ denotes the residual of the linear expansion for the exponential term. Thanks to Newton-Raphson algorithm convergence properties, we can state that there exists some integer K such that:

$$\widetilde{\mathcal{P}}([\phi, N_{\mathrm{p}}]) \approx \overline{\mathcal{P}}_{\phi}^{K}([\phi, N_{\mathrm{p}}]) \tag{3.19}$$

so that the composition of $\mathcal{C}$ and $\widetilde{\mathcal{P}}$ can be expressed in terms of linear problems.

Thanks to the reformulation described in this section, we can transform the solution of the nonlinear coupled problem for the electric subsystem in a set of linear PDE problems, as also shown in Figure. 3.2. Next section describes how the last step towards the formulation as a linear algebraic system, namely discretization, is performed.

3.4 Finite Volumes discretization for elliptic problems

In order to be numerically solved, the problems (3.18), (3.6b), (3.6c) and (3.6d) need to be discretized in space and transformed in linear systems: this is achieved in the current work by means of the finite volumes method (see e.g. [18]). Since the considered equations all fall under the elliptic category, we will present the discretization method for a generic diffusion-advection-reaction problem in the spatial domain Ω (as defined in Sect. 3.1) for the unknown u:

$$\begin{cases} \nabla \cdot (-A\nabla u + \mathbf{B}u) + Cu = f & \text{on } \Omega \\ u = g & \text{on } \Gamma_{\mathrm{D}} \\ \partial_{\mathbf{n}} u = h & \text{on } \Gamma_{\mathrm{N}}, \end{cases} \tag{3.20}$$

where A, $\mathbf{B}$ and C are possibly nonuniform diffusion, advection and reaction coefficients respectively and f is the source term, all defined from Ω onto $\mathbb{R}$ or $\mathbb{R}^3$, g and h are the boundary terms, defined from $\Gamma_{\mathrm{D}}, \Gamma_{\mathrm{N}}$ respectively onto $\mathbb{R}$, with $\partial\Omega = \overline{\Gamma_{\mathrm{D}}} \cup \overline{\Gamma_{\mathrm{N}}}$, and $\partial_{\mathbf{n}}$ is the outward normal component of the gradient operator.

In order to perform a space finite volume discretization of equation (3.20), a mesh $\mathscr{T}$ of Ω is introduced. The mesh is such that $\overline{\Omega} = \bigcup_{K \in \mathscr{T}} \overline{K}$, where an element of $\mathscr{T}$, denoted by K, is a polyhedral open subset of Ω and is called a *control volume* or cell. Assumptions on the meshes will be needed for the definition of the schemes; we refer to [18] for detailed treatment of this topic, and only describe here the geometrical entities which we will be using:

- cell center $\mathbf{x}_K$ is a point in the cell;
- face $K|L$ is the common face between cells K and L;
- neighborhood $\widehat{K}$ of a cell K is the set of cell which share a face with K;
- cell distance $d_{K,L}$ is the distance between $\mathbf{x}_K$ and $\mathbf{x}_L$;
- face center $\mathbf{x}_{K|L}$ is the point of intersection between $K|L$ and the line joining $\mathbf{x}_K$ and $\mathbf{x}_L$;
- cell measure $m(K)$ is the volume of cell K;
- face measure $m(K|L)$ is the surface of $K|L$;
- normal vector $\mathbf{n}_{K|L}$ is the unit vector normal to $K|L$ pointing from K towards L. A mesh is called orthogonal, if $\mathbf{x}_K$ and $\mathbf{x}_L$ are chosen in order to verify $\mathbf{n}_{K|L} = \frac{(\mathbf{x}_L - \mathbf{x}_K)}{d_{K,L}}$.

The discrete unknowns will be denoted by $u_K \in \mathbb{R}$, $K \in \mathscr{T}$. The value u_K is expected to be some approximation of u on the cell K (the average value, the value at $\mathbf{x}_K$, or else). The basic principle of the classical finite volume method is to integrate equation (3.20) over each cell of the mesh. One obtains a conservation law written for the volume K:

$$\int_{\partial K} (-A\partial_{\mathbf{n}} u + B_{\mathbf{n}} u) \mathrm{d}s + \int_K Cu \mathrm{d}\mathbf{x} = \int_K f \mathrm{d}\mathbf{x}. \tag{3.21}$$

The remaining step in order to define the finite volume scheme is therefore the approximation of the "flux", $-A\nabla u + \mathbf{B}u$, across the boundary ∂K of each control volume, in terms of the discrete values $\{u_L, L \in \mathscr{T}\}$. More precisely, omitting the terms on the boundary of Ω, the exchange term (from K to L) $\int_{K|L}(-A\nabla u + \mathbf{B}u) \cdot \mathbf{n} \mathrm{d}s$ is approximated by some quantity $F(K, L, u_K, u_L)$ called *numerical flux*.

The approximation of the diffusion part is straightforward: if $A_{K|L}$ denotes an approximation of A on the face (e.g., $A(\mathbf{x}_{K|L})$, or an interpolation of $A(\mathbf{x}_K)$ and $A(\mathbf{x}_L)$), then a suitable approximation of the diffusion term is:

$$\int_{\partial K} -A\partial_{\mathbf{n}} u \mathrm{d}s \approx \sum_{L\in\widehat{K}} -m(K|L)A_{K|L}\frac{u_L - u_K}{d_{K,L}}. \tag{3.22}$$

As for the convective term, different choices are possible. In general, one of the most used scheme is the *upwind* discretization, which is less accurate than interpolating on the edges but allows for unrestricted stability of the solution. The scheme reads:

$$\int_{\partial K} B_{\mathbf{n}} u \mathrm{d}s \approx \sum_{L\in\widehat{K}} m(K|L)\mathbf{n}_{K|L} \cdot \mathbf{B}_{K|L}\left(H^+_{K|L}u_K + (1 - H^+_{K|L})u_L\right), \tag{3.23}$$

being $\mathbf{B}_{K|L}$ a suitable approximation of the transport field on the face $K|L$, and:

$$H^+_{K|L} = \begin{cases} 1 & \mathbf{n}_{K|L} \cdot \mathbf{B}_{K|L} \geqslant 0 \\ 0 & \mathbf{n}_{K|L} \cdot \mathbf{B}_{K|L} < 0. \end{cases} \tag{3.24}$$

This last approach guarantees that $F(K, L, u_K, u_L) = -F(L, K, u_L, u_K)$ for any pair K, L of neighboring cells. The reaction term becomes

$$\int_K Cu\mathrm{d}\mathbf{x} \approx m(K)C_K u_K, \tag{3.25}$$

while the RHS is defined as:

$$\int_K f \mathrm{d}\mathbf{x} \approx m(K) f(\mathbf{x}_K) =: f_K. \tag{3.26}$$

Combining all the latter equations, we obtain the linear system:

$$\begin{cases} \sum_{L \in \mathscr{T}} a_{K,L} u_L = f_K & \\ a_{K,L} = 0 & \forall L \neq K, \quad L \notin \widehat{K} \\ a_{K,L} = \left(-\frac{A_{K|L}}{d_{K,L}} + H^+_{L|K} \mathbf{n}_{K|L} \cdot \mathbf{B}_{K|L} \right) m(K|L) & \forall L \in \widehat{K} \\ a_{K,K} = m(K) C_K + \sum_{L \in \widehat{K}} \left(\frac{A_{K|L}}{d_{K,L}} + H^+_{K|L} \mathbf{n}_{K|L} \cdot \mathbf{B}_{K|L} \right) m(K|L) & \forall K. \end{cases} \tag{3.27}$$

Schemes with higher order than the one presented exist, but are not covered here. For this topic, as well as for how boundary conditions can be introduced, we refer once more to [18]. Next section will make use of the algebraic formulation in (3.27) for introducing the idea lying behind the PISO method, which has been used in the solution of the fluid dynamics subsystem.

3.5 Numerical solution of Navier-Stokes equations

This section presents the inexact factorization approach which lies under the PISO method, which is adopted for velocity and pressur approximation in this work.

Navier-Stokes nonlinear problem (3.6c) can be approached with fixed point iteration techniques as the one presented for the electric subsystem: a problem in wich the current estimation for velocity works as transport field (Oseen problem) can be solved until convergence is reached. Nonetheless, the particular formulation featuring the incompressibility constraint produces, via discretization, a system of the following form:

$$\begin{bmatrix} A & B \\ B' & 0 \end{bmatrix} \begin{bmatrix} \mathbf{v}_K \\ \mathbf{p}_K \end{bmatrix} = \begin{bmatrix} \mathbf{f}_1 \\ \mathbf{f}_2 \end{bmatrix}, \tag{3.28}$$

where $\mathbf{v}_K$ and $\mathbf{p}_K$ represent the cell values of velocity and pressure, the right hand side terms $\mathbf{f}_1$, $\mathbf{f}_2$ the discretization of the source terms, while A and B arise from the differential operators, like in (3.27). In particular, A represents the diffusion-advection-reaction operator while B derives from the gradient, and B' from the divergence.

The algebraic approach consists in computing a blockwise LU decomposition of the entire matrix as first step:

$$\begin{bmatrix} A & B \\ B' & 0 \end{bmatrix} = \underbrace{\begin{bmatrix} A & 0 \\ B' & -B'A^{-1}B \end{bmatrix}}_{L} \underbrace{\begin{bmatrix} I & A^{-1}B \\ 0 & I \end{bmatrix}}_{U}. \tag{3.29}$$

Then, as a second step, the exact factors are approximated with inexact but simpler ones $\hat{L}$ and $\hat{U}$, where some of the blocks, and in particular the occurences of A, leave place to approximated matrices:

$$\begin{bmatrix} A & B \\ B' & 0 \end{bmatrix} \approx \underbrace{\begin{bmatrix} C & 0 \\ B' & -B'HB \end{bmatrix}}_{\hat{L}} \underbrace{\begin{bmatrix} I & C^{-1}B \\ 0 & Q \end{bmatrix}}_{\hat{U}} = \begin{bmatrix} C & B \\ B' & \underbrace{B'C^{-1}B - B'HBQ}_{\text{continuity error}} \end{bmatrix}. \tag{3.30}$$

Different choices are possible for the matrices C, H and Q (e.g. trying to minimize the error introduced in the continuity equation, highlighted in the formula above), giving rise to several different methods. Covering all of them is beyond the purpose of this work, so that we refer to specialized CFD literature (e.g. [21, 59, 60]). Nonetheless, it is interesting to see how the new formulation allows for staggered solution for pressure and velocity. In fact, LU factorization allows for a two-step solution of the linear system:

$$\begin{cases} \hat{L}\begin{bmatrix}\mathbf{v}_K^* \\ \mathbf{p}_K^*\end{bmatrix} = \begin{bmatrix}\mathbf{f}_1 \\ \mathbf{f}_2\end{bmatrix} \\ \\ \hat{U}\begin{bmatrix}\mathbf{v}_K \\ \mathbf{p}_K\end{bmatrix} = \begin{bmatrix}\mathbf{v}_K^* \\ \mathbf{p}_K^*\end{bmatrix}, \end{cases} \tag{3.31}$$

and with a further expansion via successive (blockwise) forward and backward substitution:

$$\begin{cases} \mathbf{v}_K^* = C^{-1}\mathbf{f}_1 \\ (-B'HB)\mathbf{p}_K^* = \mathbf{f}_2 + B'\mathbf{v}_K^* = \mathbf{f}_2 + B'C^{-1}\mathbf{f}_1 \\ Q\mathbf{p}_K = \mathbf{p}_K^* \\ \mathbf{v}_K = \mathbf{v}_K^* - C^{-1}B\mathbf{p}_K. \end{cases} \tag{3.32}$$

A very interesting reinterpretation is possible for the $(-B'HB)$ matrix if H is chosen as diagonal: H can be seen as a "diffusion coefficient" discretization and $(-B'HB)$ becomes the associated stiffness matrix (since B is the discrete counterpart of the operator ∇).

In the PISO method, C is taken as the diagonal of A, H is the inverse of C, while $Q = ((B'HB)^{-1}B'HAHB)^{-1}$ can be decomposed in order to obtain linear problems with the same structure as $(3.32)_2$. In the end, this means the solution $\begin{bmatrix}\mathbf{v}_K, \mathbf{p}_K\end{bmatrix}'$ is obtained via a cycle of successive estimations for $\mathbf{v}_K$, solutions of Poisson-like problems for $\mathbf{p}_K$, and corrections on the estimated $\mathbf{v}_K$.

This cycle takes the place of the operator $\mathcal{F}$ presented in Sect. 3.2, and together with the counterparts of $\mathcal{E}$ (or, more precisely, $\mathcal{C}$ and $\overline{\mathcal{P}}$) and $\mathcal{T}$ derived as in Sect. 3.4 enters in the algorithm represented in Fig. 3.1. The algorithm has been implemented as an OpenFOAM® solver, and the results of some simulations are presented in next chapter.

Chapter 4

Numerical simulations and results

The algorithm described in Chapter 3 has been implemented for simulation as a solver in the finite volume library OpenFOAM® [57], with the help of the library `swak4Foam` [28] for handling the boundary conditions, while meshes were produced by `gmsh` [23].

Three benchmark test cases have been chosen in the literature, where detailed data about the geometry of the devices, the experimental measurements and, where applicable, the results of numerical simulations are provided. Comparison between our results and the ones found in literature will be presented with regard to different quantities, both global or local: total current prediction of the model, current-voltage characteristics, total airflow through a surface, airflow-voltage and airflow-current characteristics, maximum temperature, temperature profiles over a surface.

Two of the benchmarks concern with simple devices (a duct geometry with electrodes installed) designed to work as EHD pumps, and therefore the reference also provides flow rate measurements. The third one is instead a simple hot-spot cooler (an electrode installed next to a heating plate on a flat surface) and the reference provides electrical and thermal data.

In particular, in the first case of Section 4.1 we will describe in more detail how the functional iterations in the algorithm are controlled, in the second case of Section 4.2 we will compare different BC models with particular regard to the hydrodynamic quantities, and in the third case of Section 4.3 we will address a problem where thermal data are

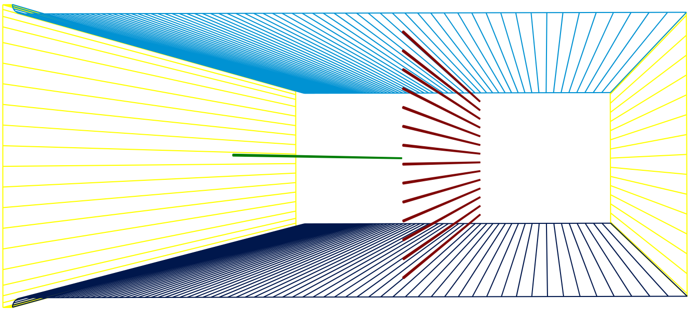

Figure 4.1: Geometry representation for Benchmark 1: 3D representation of the duct. In red the collecting grid, in blue the metal walls, in green the emitting electrode, yellow planes represent inlet and outlet sections.

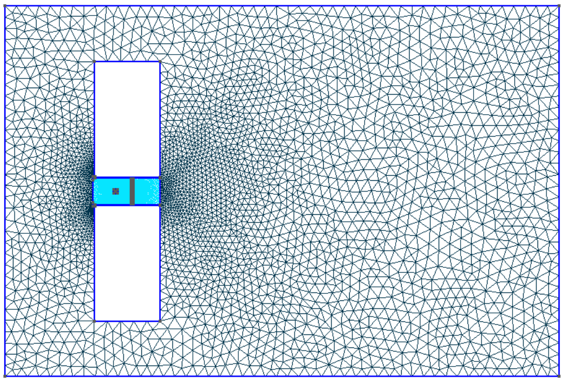

Figure 4.2: Benchmark 1: Global mesh, composed of the internal (cyan) and external (black) region of the computational domain.

available.

4.1 Forced flow in a parallel duct

Benchmark 1 geometry is taken from [36]. The setup, depicted in Figure 4.1, consists in three collectors, two of which are metal plates, acting as duct walls as well, while one is a wire grid, and of a single wire being the corona emitter. All the wires have the same diameter (50µm), and the duct dimensions are 15 × 36 × 277mm. The presence of the grid allows for a slightly steeper decay of potential on one side of the emitter, resulting in a net force on the fluid which drives it towards the grid itself, as shown in Figure 4.8. The symmetry of the domain allows for the treatment of this case as a 2D problem. We will go trough the results for this geometry discussing some algorithmic aspects, and will concentrate on the application of different models later on.

The first problem which we had to address, is that obtaining an effective flow-rate estimation was not possible by using the usual setup adopted for confined flows, that is imposing velocity value at the inflow and a null-stress at the outflow. In fact, this would have imposed the total flow-rate thanks to the incompressibility constraint. In order to provide the necessary degree of freedom, then, the duct domain was enriched by an "external room" (as shown in Figure 4.2) featuring a coarser mesh, except for the regions near the channel inlet and outlet. This way, by adding relatively few additional unknowns to the problem, the freedom for the velocity profile to adjust to the source without infringing the incompressibility constraint.

Meshing step is particularly important near the emitting wire, where the gradient of the electric potential is expectedly very large. The mesh was not adaptively refined, but the mesh size near the wire was chosen small enough to provide an adequate definition on the electric potential; in other words, if we wanted to be able to resolve electric potential differences as small as, e.g., 10V, and expected electric field peaks of the order of 10MV as Peek's law suggests, the first few mesh cells near the electrode would have measures of the order of 1μm. Another issue, as shown in Figure 4.3, is that unstructured meshes behave poorly when the boundary conditions impose abrupt variations (e.g. in (2.22)). In those situations, even a small difference on the estimated value for the electric field could lead to a very different outcome in terms of ion or current density, and then in turn of velocity; this occurrence has been avoided with the employment of almost structured layers in the boundary vicinity.

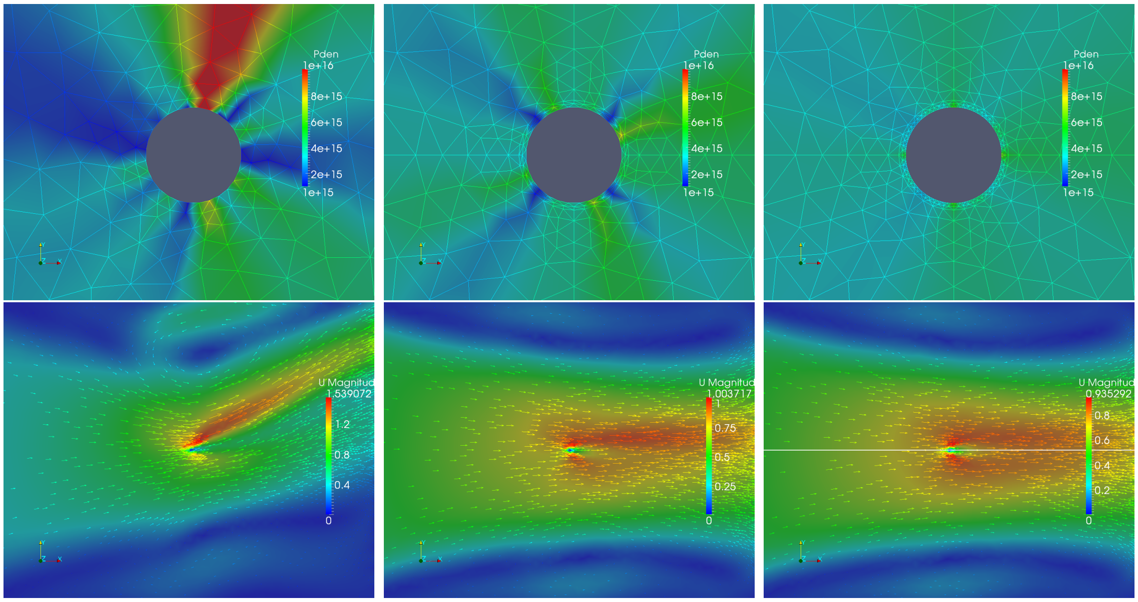

Figure 4.3: Comparison of different meshing algorithms of the domain region near the emitter: ion density in the top row, velocity in the bottom row. Left to right, unstructured mesh and two different structured ones. All results shown are obtained with boundary condition as in (2.22).

With regard to linear algebra OpenFOAM® allows for choosing among some embedded iterative solvers, and standard convergence criteria based on the ratio of residual reduction are used. In our tests the degrees of freedom were in general in the order of 10^4 for 2D simulations ($\approx$ 22000 prisms for this particular benchmark) and we chose the multigrid `GAMG` solver, which proved faster than (bi-)conjugate gradient solver.

The different iterative cycle in the problem, described in Sections 3.2, 3.3 and 3.5, are subject to termination conditions which we did not specify yet. While performing the simulations we noticed that, since small time steps are employed, the main loop for time advancing produced non negligible variations on the unknowns only in the first iteration. We consider this to happen due to both the arrangement of the subproblems solution in the algorithm flow and the different time scales of the physical phenomena involved: forcing term needs enough time to produce notable velocities, and convection needs even more

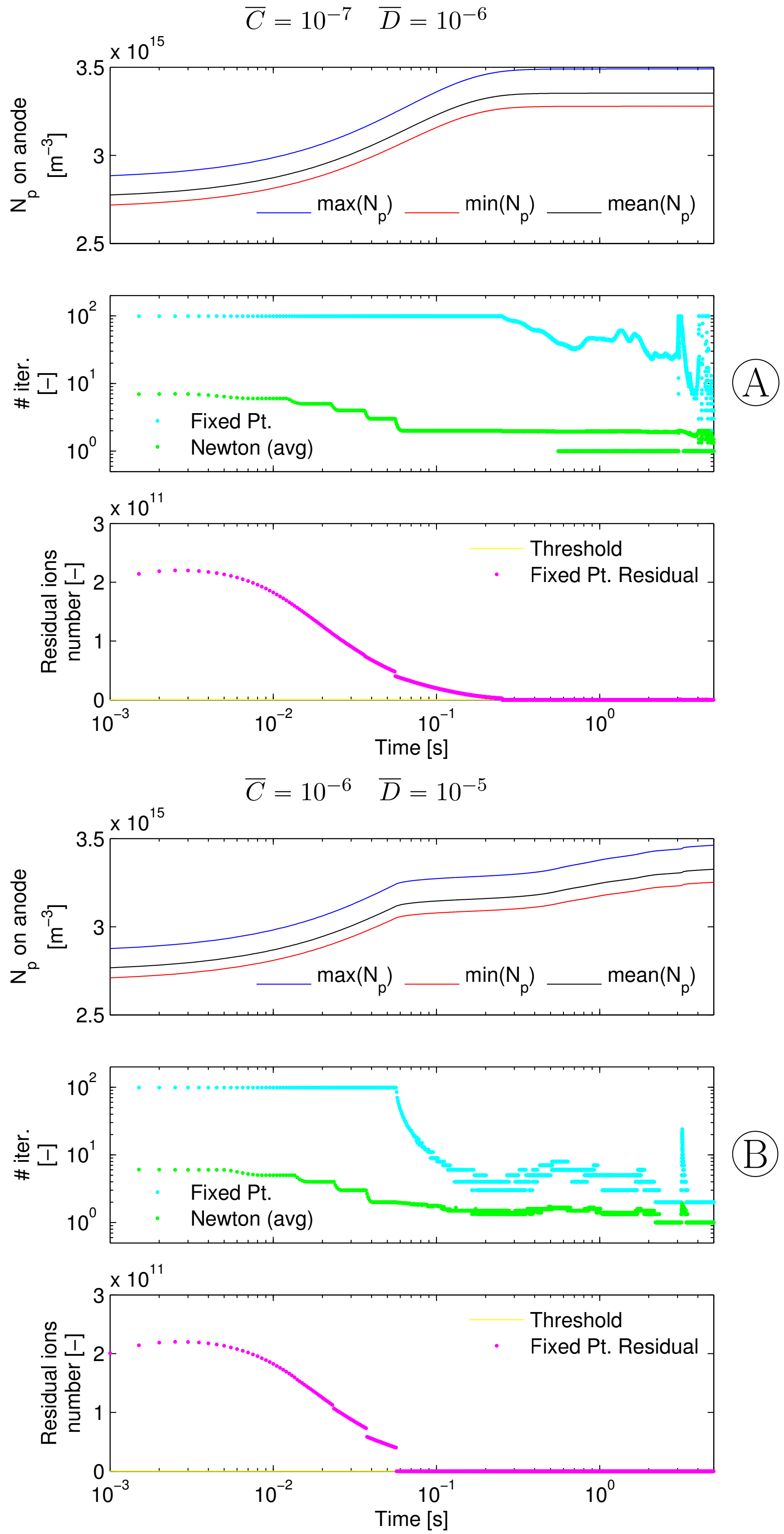

Figure 4.4: Number of iterations and final residual for Benchmark 1 with small tolerances. C and D refer to (4.1) and (4.2) respectively.

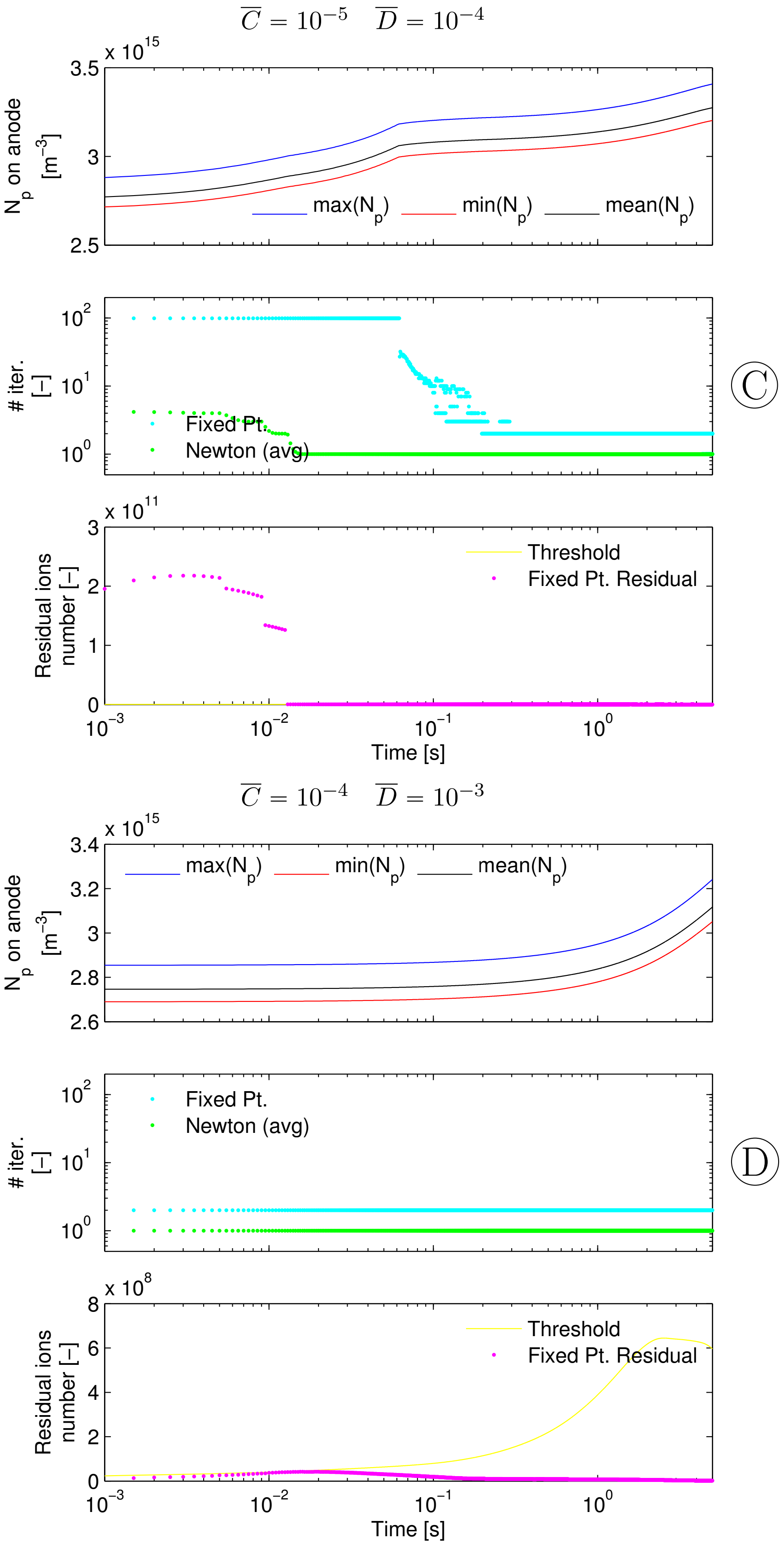

Figure 4.5: Number of iterations and final residual for Benchmark 1 with large tolerances. $\overline{C}$ and $\overline{D}$ refer to (4.1) and (4.2) respectively.

to consistently reduce temperature. In conclusion, we decided to only perform one main loop iteration for each time step *and* maintain the time step short, mainly because for the application of the predictive conditions large time steps lead to numerical instabilities, which we will describe later on.

Figures 4.4 and 4.5 show the result of using different threshold values for terminating the electric fixed point iterations introduced in Section 3.3; the simulations are performed with the uniform boundary condition on the corona electrode. The termination criterion applied for the fixed point iterations, according to the notation in Figure 3.2, is the following:

$$\int_{\Omega} N_{\mathrm{p}}^{k+1} - N_{\mathrm{p}}^{k} \exp\left(\frac{\phi^{k+1}-\phi^{k}}{\phi_{\mathrm{E}}}\right) \mathrm{d}\mathbf{x} \leqslant \overline{C} \int_{\Omega} N_{\mathrm{p}}^{k+1} \mathrm{d}\mathbf{x} \tag{4.1}$$

where the left and right hand side is what we called “residual” and “threshold” respectively in the graphs; moreover, a maximum number of iterations of 99 has been imposed. This particular form has been chosen to enforce not only the new values of N_{p} and ϕ to be near the fixed point, but also to make the nonlinear version of Poisson’s problem in (3.17) as consistent as possible with the original one in (3.14). The termination criteria for the Newton iterations in nonlinear Poisson equation reads instead:

$$\int_{\Omega} |\delta\phi| \mathrm{d}\mathbf{x} \leqslant \overline{D} \int_{\Omega} |\phi| \mathrm{d}\mathbf{x}. \tag{4.2}$$

Simulations which Figures 4.4 and 4.5 refer to, were run with an initial condition for ion density $N_{\mathrm{p}} = 0$ and an imposed voltage of 5kV, so that a transient in which most of the charge needs to be injected in the domain is present. This transient is visible in particular in the first three cases shown in Figures 4.4 and 4.5, where the ion density on the wire grows to enforce the total imposed current density, as the electric field diminishes due to shielding; the simulation with the lowest threshold shows a smooth growth, which is less the case for the remaining two. In the case with the highest tolerance, instead, the electric potential and field (and in turn the injected charge) adapt too slowly and the transient is delayed. Convergence of Newton sub-cycle introduced in Section 3.3 is also slower in the beginning, in all three "good" cases, since the initial guess is poorer and the ion density source term is subject to larger changes, but becomes much quicker when the ion densities approach steady state. Table 4.1 provides a comparison of the four simulations, denoted by letters A, B, C and D, also in terms of computation time and of average outlet velocity: here we can find further confirmation of our initial idea that the last, more loose simulation is quite definitely inaccurate with respect to the other ones.

Graphs in Figure 4.6 present the outcome of using a different cap on the iteration number for the fixed point loop. The purpose of terminating the cycle early is to speed up towards a steady state, in the vicinity of which convergences are faster as we already showed. The graphs in Figure 4.6 compare to simulation B in Figure 4.4, and the maximum iterations are reduced to 50 and 10 respectively. The former case presents a behavior quite similar to the 99 case, even if the threshold is not met until around double the time, while the latter case propagates the error further on in a similar fashion as case D in Figure 4.5. Taking a look back at Table 4.1, where the two cases are denoted E and F, one can notice that computation times with this second approach are not really reduced, but on the other hand also the outlet velocity is quite similar to the cases where more iterations are allowed.

A third way we used to try to obtain faster simulations is to "turn off" the electrical part once it reaches an almost steady state: this can be effective because the small changes in current and electric field have no huge effect on velocity, and avoiding the residual computation, even if the fixed point and Newton cycle would perform no iteration, can

---

[1] Computation time is approximate and refers to simulations ran on a laptop computer with Intel® Core™ i7 2630QM Processor, 4GB DDR3 1333 MHz RAM

Table 4.1: Summary of the simulations from Figure 4.4 and 4.6.

Sim.	Fixed point cycle tolerance ($\log_{10}$)	Newton iteration tolerance ($\log_{10}$)	Maximum iterations number	Simulation time [s] [1]	Average airflow (4s to 5s) compared to A
A	-7	-6	99	165255	100 %
B	-6	-5	99	55542	94.6 %
C	-5	-4	99	35804	91.9 %
D	-4	-3	99	27518	68.9 %
E	-6	-5	50	51920	95.9 %
F	-6	-5	10	48894	98.6 %

result in time saving. We report the results of an experiment made by prolonging to a final time of 10s simulations A and B from Table 4.1 with time step increased from 0.5 to 5ms, while maintaining all the other parameters unchanged: the average outlet velocity was of 0.2713m/s and 0.2748m/s respectively, and the computation time of 3374s and 4710s. Running the prolongation of case B without solution for the electrical part turned out in 0.2741m/s average outlet velocity, but lasted only 2378s. We want to point out that this does not mean one can completely decouple the two equations since the beginning: fluid velocity plays in fact an important role in the distribution of charge overall, but small variations do not drastically change the nearly-steady behavior of the electrical system.

At last, we discuss here the application of two boundary conditions: the non predictive uniform one as in (2.18) and the ideal diode condition as in (2.22). We performed simulations at different voltages and compared the results with the ones proposed in [36]. As can be evinced from Figure 4.7, the diode-like condition produces good results in estimating current, and the parabolic trend expected as in (2.1) is met. The airflow characteristic as in Figure 4.8 is also well matched by both the simulations sets, at least in the shape of the curves, while small underestimation is present in both cases. However, we defer further examination of the boundary conditions to the following sections, where we applied them to different geometries.

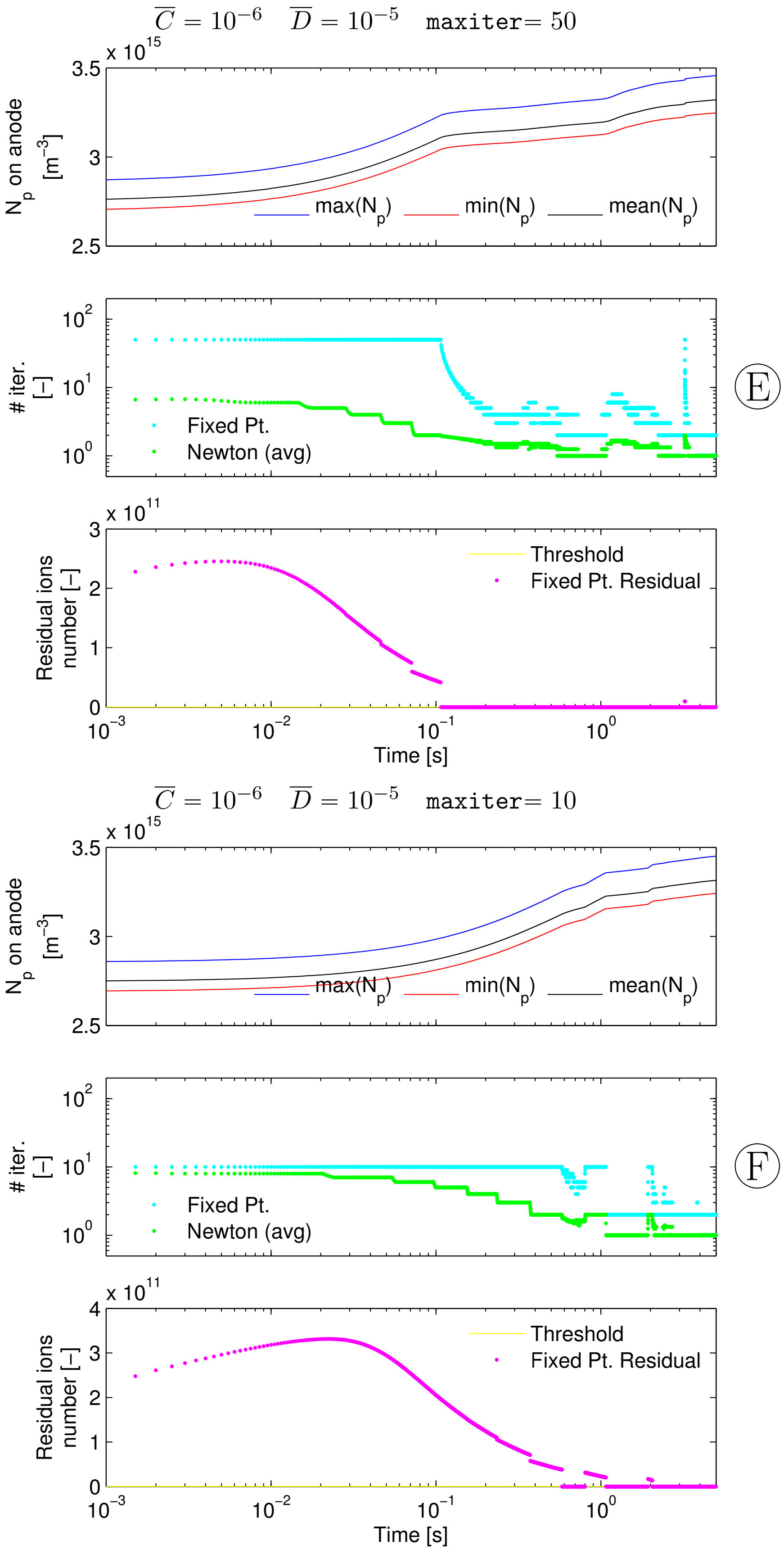

Figure 4.6: Number of iterations and final residual for Benchmark 1 with different iteration limits.

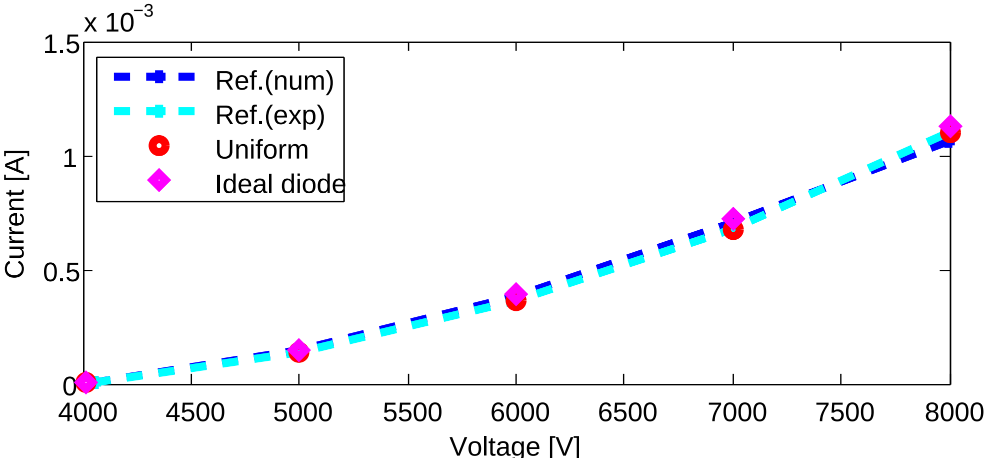

Figure 4.7: DC characteristic curve for Benchmark 1.

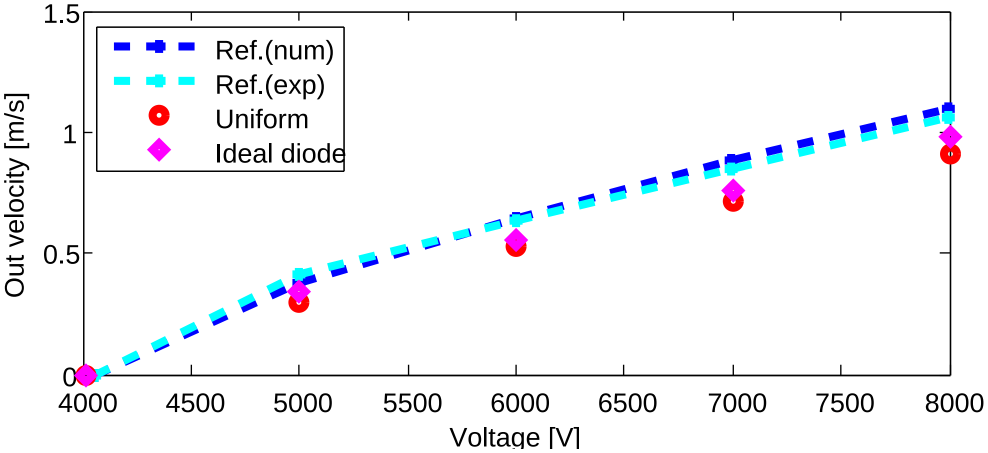

Figure 4.8: Airflow characteristic curve for Benchmark 1.

4.2 Forced flow in a converging duct

Benchmark 2 geometry is taken from [13], where EHD-forced flow in a converging duct is experimentally studied. The experimental set-up (see Figure 4.10) consists in a plexiglass (insulating) duct with two conductive plates on the horizontal sides and a 0.24mm diameter corona-emitter in the middle of the channel. The actual position of the wire in our simulations is the one marked with letter A in the reference, namely 60mm far from the 16mm wide small opening of the duct. The total length of the duct is 117mm, the width measures 33mm and the wider opening 24mm. Thanks to the symmetry of the domain, a 2D simulation has been run. As it can be appreciated by taking a look at Figure 4.9, the principle on which this particular realization of the device works is based on the creation and detachment of vortexes, generated by the EHD force field and the duct walls reaction. Asymmetric vortexes detach then, directed towards the smaller duct opening.

The experimental DC characteristic curve in Fig. 4.12 fits well the theoretical prediction of a parabolic relation, as presented in (2.1), having a convex shape and crossing the voltage axis around the $5.5-6$kV onset voltage. Three different boundary conditions (2.18), (2.22) and (2.23) have been tested in this case: we will discuss the uniform and ideal diode ones before, and then concentrate on the real diode condition. The uniform condition unsurprisingly matches the experimental data, while the ideal diode overestimates the current just slightly, maintaining a good agreement with the experiments and a similar parabolic ongoing; the value for the onset field for the imposition of (2.22) has been chosen by simulating the “onset case”, namely imposing the empirically measured onset voltage allowing no current, and then sampling the electric field on the electrode.

A comparison of measured and computed velocity averages on the outlet section is provided in Fig. 4.13. The uniform condition provides a seemingly linear relation between velocity and applied voltage, while measured velocities seem to saturate quite early. The

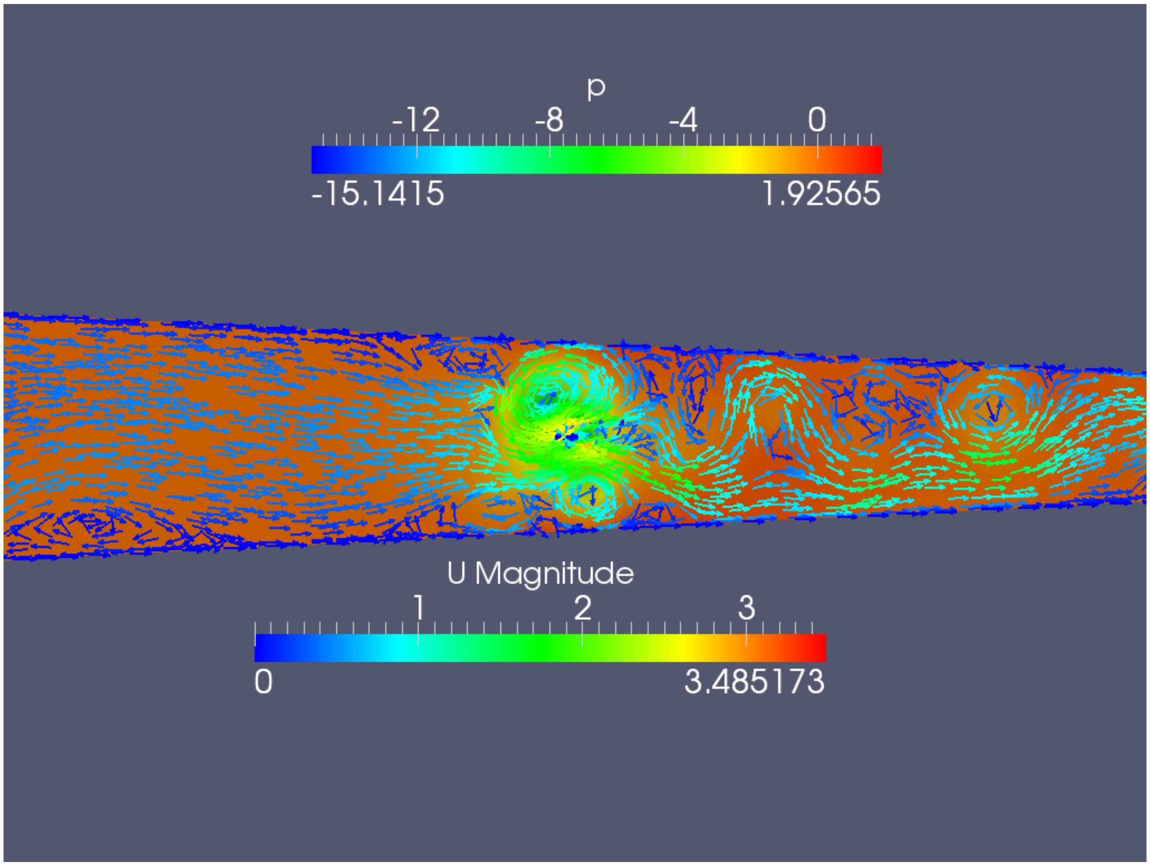

Figure 4.9: Instantaneous velocity field and pressure obtained at 7kV imposed voltage.

diode-like conditions seem to better agree with the reference, at least for higher voltages.

The poor fitting of the data at lower voltages can be explained by checking the relation between power and flow rate, as in Figure 4.14: this graph shows a far better matching, and this happens because in the low voltage simulations, where the even small errors on the current are comparable with the current value itself, appreciably different powers are applied on the flow field. This in turn justifies the concern in having good current estimations for a reliable modeling of the electrohydrodynamic phenomena.

Two different curves are presented in Figure 4.13 for the real diode model. The first one has been run with parameters E_{ref} and $\widetilde{N_{\mathrm{p}}}$ of 6.5×10^5V/m and 5×10^6m^{-3} respectively,

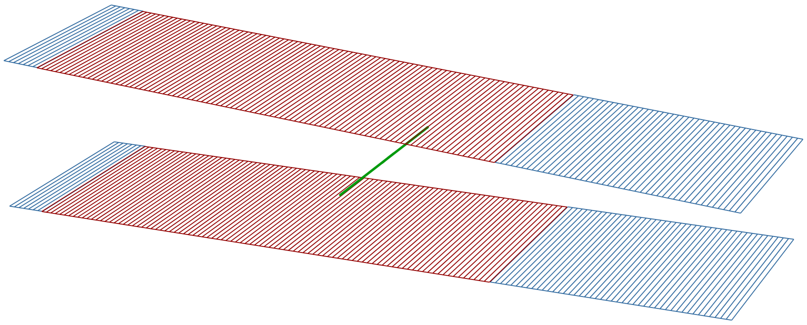

Figure 4.10: Blue part represents insulating walls, red represents collecting grounded plates, green represents the emitter

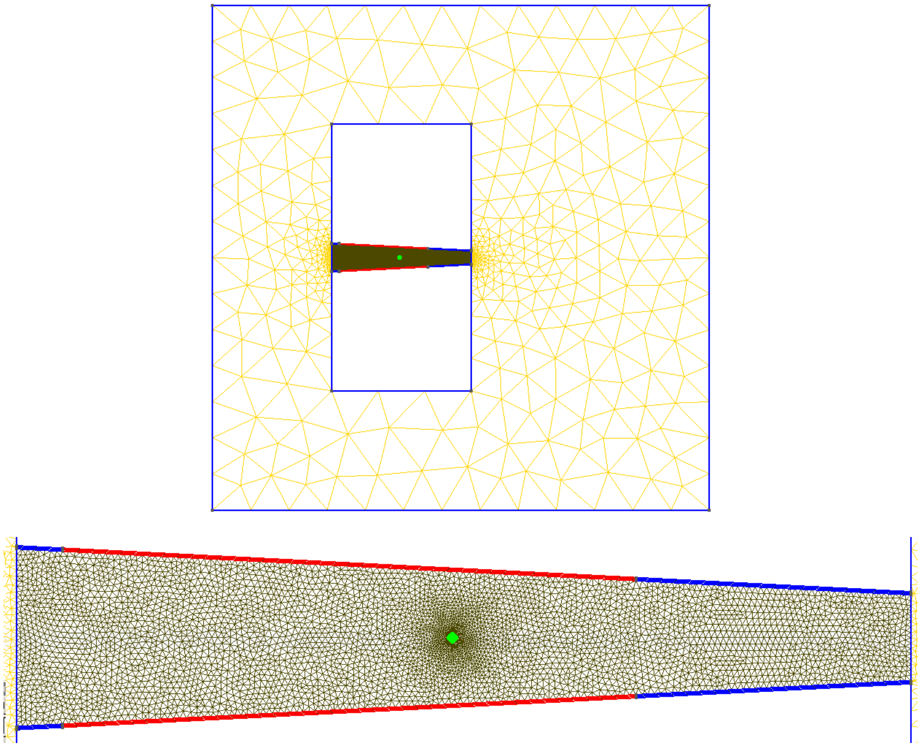

Figure 4.11: Mesh details from Benchmark 2. Left, the entire computational domain; right, detail of the duct.

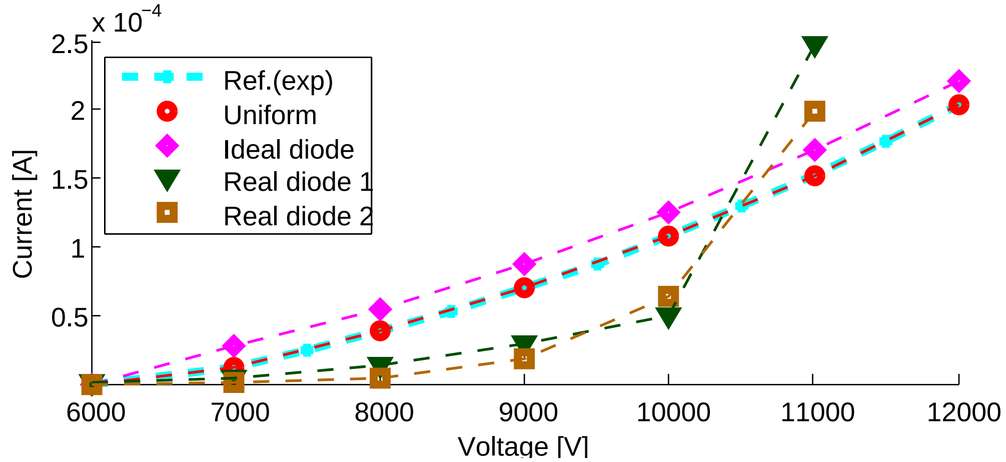

Figure 4.12: DC characteristic plot for the first benchmark case, where a comparison between the experimental data and the result of applying (2.18), (2.22) and (2.23) is provided.

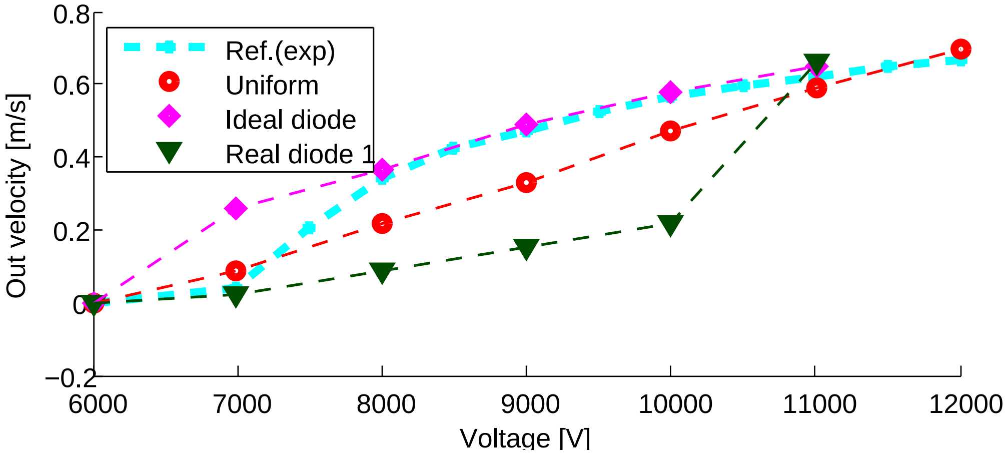

Figure 4.13: Airflow plot for Benchmark 2, with different applied voltages.

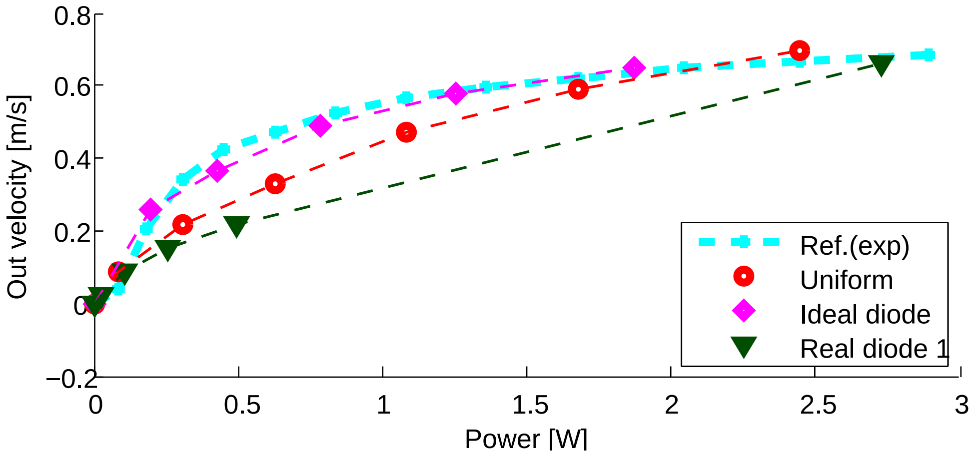

Figure 4.14: Airflow vs. power plot for Benchmark 2.

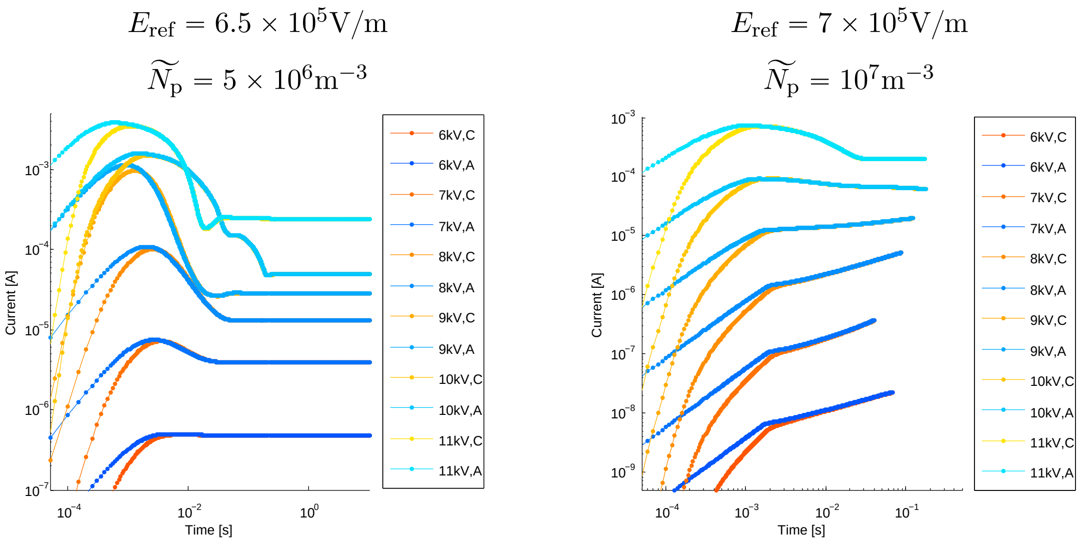

$E_{\mathrm{ref}} = 6.5 \times 10^5 \mathrm{V/m}$

$\widetilde{N}_{\mathrm{p}} = 5 \times 10^6 \mathrm{m}^{-3}$

$E_{\mathrm{ref}} = 7 \times 10^5 \mathrm{V/m}$

$\widetilde{N}_{\mathrm{p}} = 10^7 \mathrm{m}^{-3}$

Figure 4.15: Real diode model currents with different parameters and voltage. Lines denoted A refer to anode currents, lines denoted C to cathode currents.

while in the second case the same parameters were set to 7×10^5V/m and 10^7m^{-3}. Figure 4.15 shows the trend of the current over time in both the simulation sets. For both of them, a relaxation factor on the boundary condition has been imposed between each linear system solution and the following. The factor value for the first simulation was 2×10^{-4}, but in the higher voltage cases ($\geqslant$ 10kV) this lead to instabilities evidenced by the non physical big overshooting and oscillation in the leftmost chart of Figure 4.15, so that a smaller value of 2×10^{-7} had to be used for continuing the simulations. This small value has been applied also to the simulations of the leftmost chart, which are still incomplete and far from a steady state; it can be noted that for low and medium applied voltages, the very low relaxation factor slows down rather than speeding up the current convergence to a steady value.

Fitting of the experimental values for the total current is rather poor for both the parameter sets presented. However, the second set is more promising in this regard, as already noted the currents for the medium-low applied voltages seem to maintain a steadily increasing pace, which should eventually lead to a final I-V characteristic curve more similar to the experimental one. Further assertions, though, need to be delayed until a full simulation can be analyzed and possibly a more extensive study of the parameters is undergone.

4.3 Convective cooling of a flat plate

Geometry for Benchmark 3 comes from Go et al.'s papers [24, 27]. A flat plate is resistively heated with 4W of power, and is cooled by the combined action of a bulk flow, with a velocity between 0.2 and 0.3$\frac{\mathrm{m}}{\mathrm{s}}$, and a very simple EHD blower. The blower is formed by a steel wire with 50µm diameter, placed at a vertical distance of 3.15mm from the plate, and at a variable horizontal distance upwind of a 6.35mm wide strip cooper tape, which lays on the plate acting as cathode; the geometry is depicted in Figure 4.16. Different voltages are investigated, for a time range of the order of minutes; the extension of the time range is necessary to appreciate the temperature evolution, which occurs on much bigger time scales than the electrical and dynamical phenomena.

Figure 4.17 shows a comparison of the obtained velocity and temperature fields in three different discharge regimes, with the setup as in [24]: the first "device off" case provides a reference temperature, while the other two cases simulate a near-onset and a higher voltage discharge respectively. As pointed out in the references, the purpose of the blower is to disturb the boundary layer, which is evident in the "device off" case, and thus allowing for a better "heat extraction rate" (namely an increase in the convective heat transfer

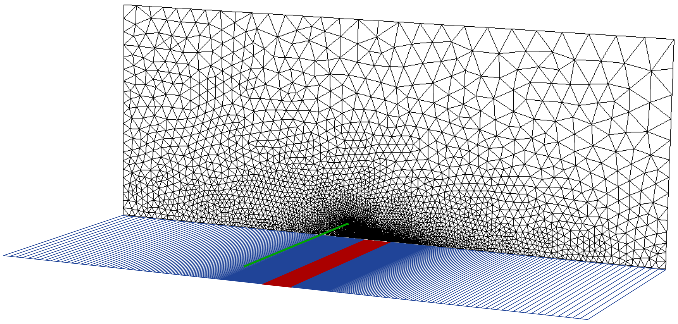

Figure 4.16: Benchmark 3: Geometry of the EHD blower. In green the emitter, in blue the insulating plate, in red the copper collector. In black on the background, the mesh used in 2D simulation.

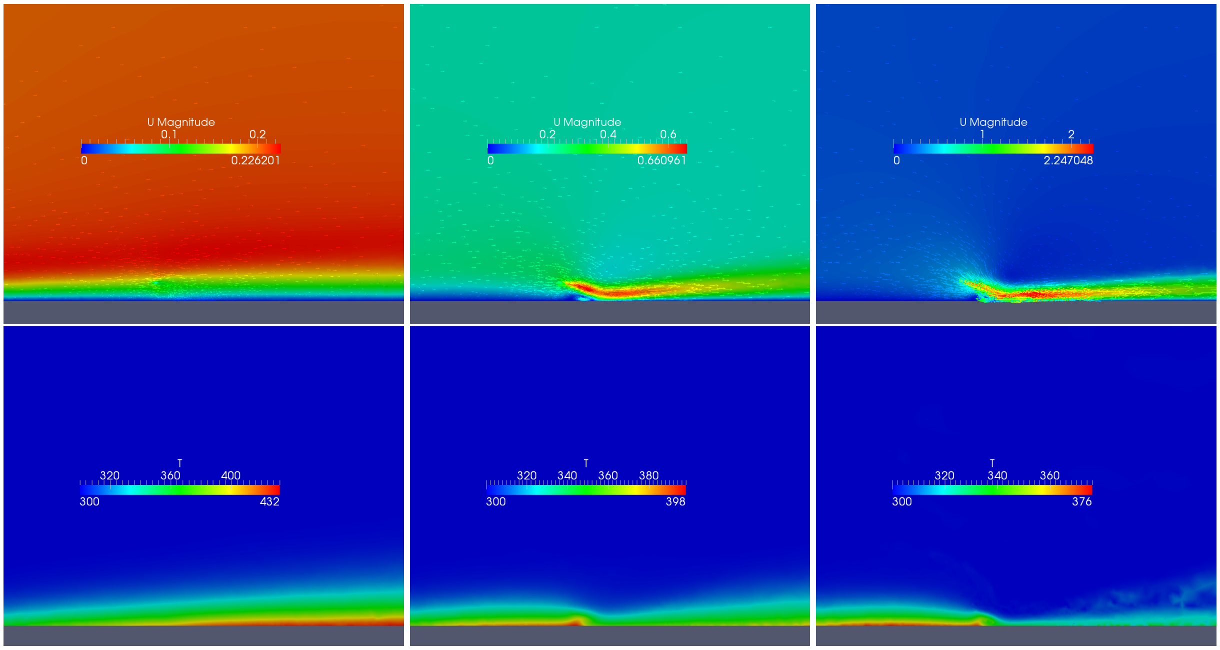

Figure 4.17: Comparison of velocity [$\frac{m}{s}$] and temperature [K] fields for three different applied voltages for the setup as in [24]. Left, device off. Center, device near onset voltage ($\approx$ 3kV). Right, high voltage regime ($\approx$ 4.6kV).

coefficient).

The subsystems in the EHD problem present strong time-multi-scale properties: the dynamics of the electrical component is very fast, while the thermal component have much longer characteristic time scale. This can be appreciated in Figure 4.18, where temperature profiles (temperature differences relative to the corresponding “device off” value) over the plate are plotted at different times. For being able to reach the end of transient states for the complete system, the simulation were carried in three different steps: at first, a very short time step was chosen, to allow the electric variables to reach an almost steady state; then the time step was increased in order for the flow field to settle; in the end, a larger time step was adopted with the purpose of reaching an approximately steady state for temperature field; those latter simulations were performed in the same way described in the end of Section 4.1, with the electrical block not active. The maximum temperature on the plate and the time step variation is shown in Figure 4.19: the initial value for temperature field is given by the solution of the steady state temperature equation with uniform velocity, thus the progressive formation of boundary layer is responsible for the increasing “device off” peak.

Figure 4.20 shows comparisons of experimental and numerical temperature profiles (both from reference and from our computations), given as in [24] in the nondimensional form of the ratio of the “device off” and the “device on” temperature increase, with respect to the incoming air: the higher the values for this nondimensional temperature, the better the enhancement of heat transfer works. The poor correspondence of both numerical profiles to the experimental data is arguably due to the imposed boundary condition, namely a uniform incoming power density summing up to 4W over the whole plate.

Figure 4.21 shows a comparison of our results (in term of total current) in simulating the work of the device from [27], with an inter-electrode horizontal distance of 4mm. This particular setup presents the most difficulties among the ones analyzed, because of its non-symmetry. Simulations were performed using three different models (2.20),(2.22) and (2.23); the uniform condition could not be applied: in fact, it lead to an accumulation of free charge on the side of the emitter opposite to the collector, which in turn made the whole system unstable. It is however necessary to point out how a uniform emission would be inherently nonphysical, as the ionizing electrons come preferably from the cathode, the electric field around the wire is much stronger in the same direction.

As a result of the mentioned facts, all the three different models produce on the wire an “active” region facing the plate, through which most of the current flows. The comparison of the curves in Figure 4.21 highlights an acceptable match of the two diode-like models with the experimental curve, while the “charge controlled current” model presents a saturation-

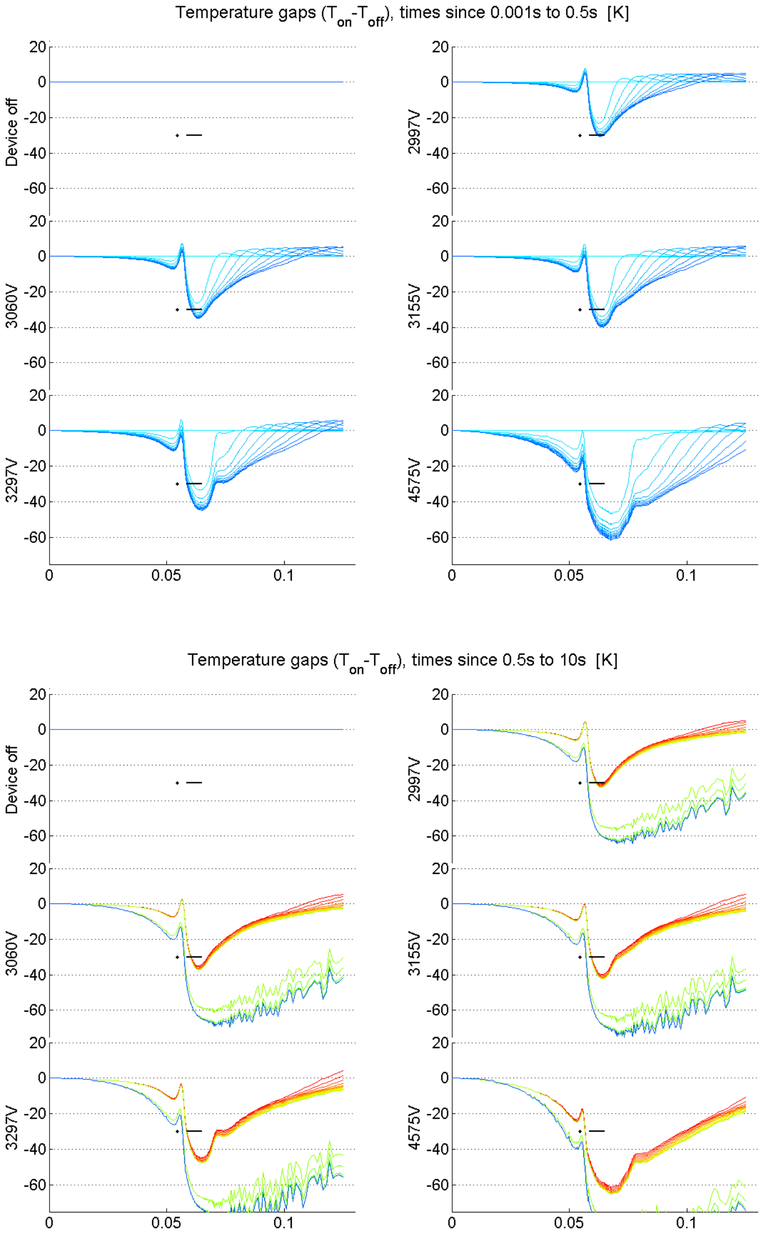

Figure 4.18: Benchmark 3: Profiles of temperature differences near the flat plate, 0.001s to 0.5s (left) and 0.5s to 10s (right). Line color ranges from cyan to blue to red to green as time grows.

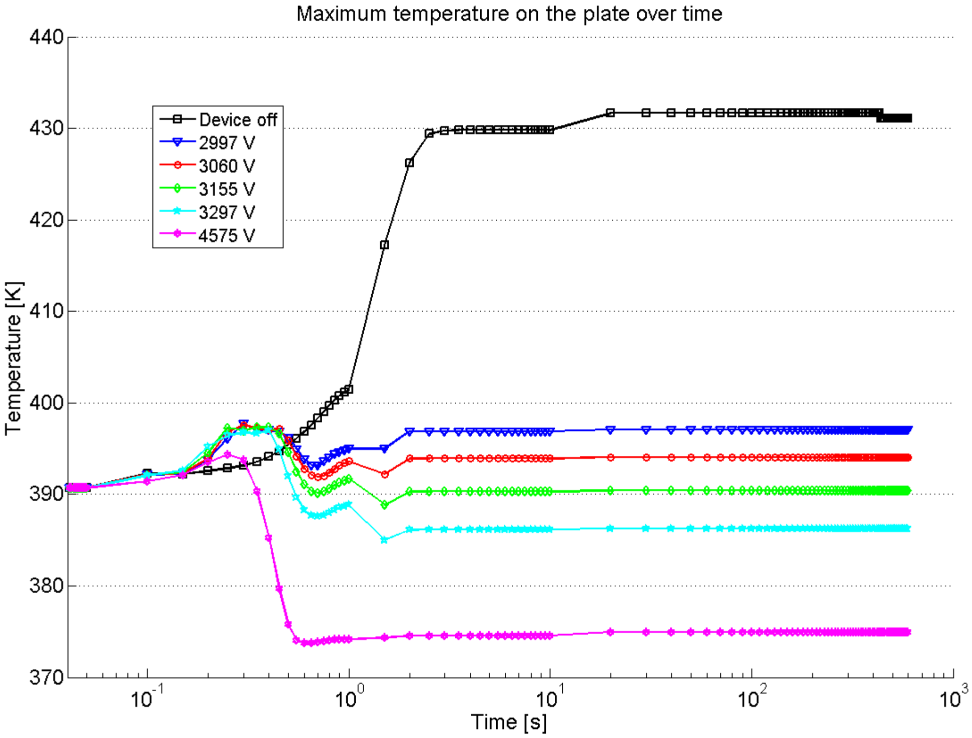

Figure 4.19: Benchmark 3: Maximum temperature on the plate over time. Logarithmic time scale helps appreciating the variation in time step.

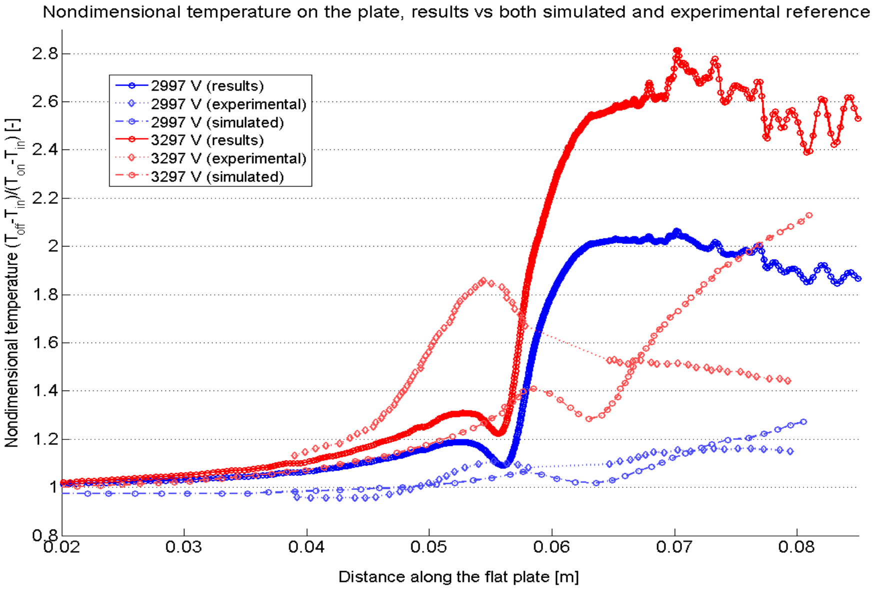

Figure 4.20: Benchmark 3: relative temperature comparison. The reference is [24], where numerical simulations results are also provided. The corona model in our computation is the ideal diode one (2.22).

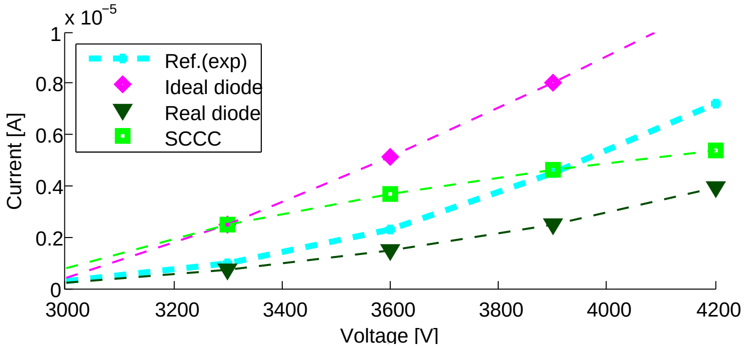

Figure 4.21: DC characteristic curve for Benchmark 3.

like ongoing. As already mentioned, the real diode model has the additional advantage of being further on adjustable for a better fitting to the data, while the ideal model cannot be modified to correct the higher voltage overestimation, without sacrificing the matching onset voltage value.

CHAPTER 5

Conclusions and outlook

This thesis is the result of the work carried out by the author as an intern at ABB Corporate Research, on the EHD enhancement of convective cooling. In particular, it deals with the mathematical modeling and simulation of the phenomena of electrohydrodynamics and corona discharge. Summarizing, the main achievements in this work are the following:

- A physical model for ElectroHydroDynamic phenomena (EHD forces and PDE system) has been introduced, applying suitable simplification that are allowed by the specific application of interest (incompressible dry air flow);
- Boundary conditions representing ion injection due to corona discharge have been studied, and both data-based and predictive models for charge injection have been formulated. Two new models have been proposed, which account for the main macroscopic features of corona discharge;
- An algorithm for the decoupling and numerical solution of the PDE nonlinear system arising from the physical model has been designed, inspired on the techniques used in different fields such as computational electronics, electrochemistry and fluid dynamics;
- The algorithm has been implemented as a solver for the OpenFOAM® library;
- The discharge models proposed have been tested and validated by comparison with experimental data obtained from scientific literature;

- The solver has been used for simulation of real industrial cases, which we did not present due to confidentiality reasons.

With particular regard to the injection models studied, which constitute the most innovative contribution of this thesis, we can conclude that:

- the uniform model can be applied to simulation of simple, symmetrical geometries only, and furthermore does not provide any prediction of the discharge;
- the space charge controlled current model is not reliable when non negligible electrical currents are present, and thus it is hardly suitable for corona discharge simulation;
- the ideal diode model has quite good prediction ability, and can be used in non symmetrical cases;
- the real diode model is promising, due to its flexibility with respect to the ideal diode model; however, it still needs to be developed with particular regard to criteria for the choice of its parameters.

Possible topics for further advancement can be:

- the definition of a physical framework for the ideal diode model, which may allow for the physical interpretation of the model parameters which, in turn, would help in the choice of their value;
- the acquisition of more accurate thermal data for comparison and benchmarking, or the development of a multiphysics model to allow better treatment of the heat transfer distribution at the solid-fluid interface;
- a parallel implementation of the OpenFOAM® solver, which would allow for faster simulations in 3D, “real life” cases; this should be rather straightforward, since

OpenFOAM® was chosen as the implementation framework in part because of its embedded parallel computing capabilities, which have not been yet exploited due to some technical issues.

List of Symbols

α Coefficient for the N_p term in the generic formulation $\alpha N_\mathrm{p} + \beta \nabla N_\mathrm{p} \cdot \mathbf{n} = \kappa$ of anode boundary condition; In general, α is a function of E_n . 26–30, 35, 36, 39, 69

$\alpha_\mathbf{T}$ First Townsend coefficient, namely the number of free electrons produced by impact ionization by one electron in a unit length path ($[\mathsf{L}^{-1}]$). 24–26

β Coefficient for the $\nabla N_\mathrm{p} \cdot \mathbf{n}$ term in the generic formulation $\alpha N_\mathrm{p} + \beta \nabla N_\mathrm{p} \cdot \mathbf{n} = \kappa$ of anode boundary condition; In general, β is a function of E_n . 26–30, 35, 36, 39, 69

$\beta_\mathbf{exp}$ Thermal expansion coefficient at constant pressure, given as $\frac{\mathrm{d}(-\ln \rho/\rho_0)}{\mathrm{d}T}|_{p=\mathrm{const.}}$ ($[\Theta^{-1}]$). 22

$\beta_\mathbf{T}$ Second Townsend coefficient in its original form, defined as the number of free electrons produced by impact ionization by one positive ion in a unit length path. ($[\mathsf{L}^{-1}]$). 25

ε Absolute electrical permittivity ($[\mathsf{M}^{-1}\mathsf{L}^{-3}\mathsf{T}^{2}\mathsf{Q}^{2}]$). 17–21, 30, 34, 36, 39–41

η Dynamic viscosity of the fluid ($[\mathsf{L}^{2}\mathsf{T}^{-1}]$). 22

$\gamma_\mathbf{T}$ Second Townsend coefficient, namely the number of free electrons released from the cathode per initial ionizing collision in the gas.($[-]$). 24–26

κ Right hand side term in the generic formulation $\alpha N_\mathrm{p} + \beta \nabla N_\mathrm{p} \cdot \mathbf{n} = \kappa$ of anode boundary condition; In general, κ is a function of E_n . 26–30, 35, 69

μ Ion mobility, namely the ratio between the drift velocity of charge carriers and the applied electric field ($[\mathsf{M}^{-1}\mathsf{TQ}]$). 18, 21, 23, 27, 29, 30, 35–37, 39

ν Kinematic viscosity of the fluid, or momentum diffusion rate, namely the ratio between the dynamic viscosity and the mass density of the gas ($[\mathsf{ML}^{-1}\mathsf{T}^{-1}]$). 22, 30, 35, 37

ϕ Electric potential ($[\mathsf{ML}^{2}\mathsf{T}^{-2}\mathsf{Q}^{-1}]$). 21, 30, 34–41, 51, 71

ρ Mass density of the fluid ($[\mathsf{ML}^{-3}]$). 17, 19, 22, 23, 30, 35, 37, 69

σ Electric conductivity, namely the ratio between the drift current density and the applied electric field ($[\mathsf{M}^{-1}\mathsf{L}^{-3}\mathsf{TQ}^{2}]$). 21

C_V Massive specific heat at costant density ($[\mathsf{ML}^{-1}\mathsf{T}^{-2}\Theta^{-1}]$). 22, 23, 30, 35, 37

D Ion diffusion rate, or diffusivity, namely the ratio between the diffusion current and the carriers density gradient ($[\mathsf{L}^{2}\mathsf{T}^{-1}]$). 21, 23, 27, 29, 30, 35–37, 39

$\mathbf{E}$ Electric field ($[\mathsf{MLT}^{-2}\mathsf{Q}^{-1}]$). 17–26, 30, 35, 37

E_n Electric field normal to a surface. 26–29, 69

$E_{\mathbf{on}}$ Treshold electric field for the onset of corona discharge. 26–29

$E_{\mathbf{ref}}$ Reference electric field. 28, 29

$\mathbf{f}$ Volumetric force ($[\mathsf{ML}^{-2}\mathsf{T}^{-2}]$). 17–20

$\mathbf{f_{EHD}}$ Volumetric EHD force, namely the force exerted on a unit volume fluid because of the electric field and free charge. 17, 20, 22, 30, 35, 37

$\mathbf{g}$ Gravity acceleration ($[\mathsf{LT}^{-2}]$). 22

i Current ($[\mathsf{QT}^{-1}]$). 16, 26, 27, 29

$\mathbf{j}$ Current density ($[\mathsf{L}^{-2}\mathsf{T}^{-1}\mathsf{Q}]$). 21–23

j_n Current density normal to a surface. 27

$j_{\mathbf{sat}}$ Saturation current density, or maximum current density which the conductor can carry. 27, 29

k Temperature diffusion rate, ($[\mathsf{M}^2\mathsf{L}^{-2}\mathsf{T}^{-3}\Theta^{-1}]$). 22, 23, 30, 35, 37

$k_{\mathbf{B}}$ Boltzmann constant, valued $1.3806503 \times 10^{-23}\mathrm{kgm}^2\mathrm{s}^{-2}$. 39

$N_{\mathbf{p}}$ Number density of positive ions ($[\mathsf{L}^{-3}]$). 17, 18, 20, 21, 23, 26–30, 34–41, 51, 69, 71

p Pressure in the fluid ($[\mathsf{ML}^{-1}\mathsf{T}^{-3}]$). 22, 24–26, 30, 34–38, 44, 45, 69, 71

q Elementary electrical charge, or electrical charge of a proton ($[\mathsf{Q}]$). 18, 20, 21, 23, 27, 29, 30, 34–37, 39–41

T Temperature ($[\Theta]$). 22, 23, 30, 34–39, 69, 71

$T_{\mathbf{ref}}$ Reference temperature, or the temperature used in gas properties computation. 22

t Time($[\mathsf{T}]$). 21, 30, 34–37, 39

$\bar{t}$ Final time. 30, 33, 34

$\mathbf{u}$ Solution vector for the system of PDEs, either as a function of time with values in $\mathbb{U}$ or as an element of $\mathbb{U}$ when time is fixed. Defined as $[\phi, N_{\mathrm{p}}, \mathbf{v}, p, T]$. 33, 34, 36, 71

$\mathbb{U}$ The function space in which $\mathbf{u}$ is found. 33, 34, 36, 38, 71

$\mathbf{v}$ Velocity field in the fluid ($[\mathsf{LT}^{-1}]$). 21–23, 30, 34–39, 44, 45, 71

V Applied voltage, or the electric potential ϕ applied to an electrode ($[\mathsf{ML}^2\mathsf{T}^{-2}\mathsf{Q}^{-1}]$). 16, 30, 34, 36, 39, 40

$V_{\mathbf{on}}$ Corona onset voltage. 16, 26

Bibliography

[1] K. Adamiak and P. Atten. “Simulation of corona discharge in point-plane configuration”. In: *Journal of Electrostatics* 61.2 (2004), pp. 85–98.

[2] S. O. Ahmedou and M. Havet. “Analysis of the EHD enhancement of heat transfer in a flat duct”. In: *Dielectrics and Electrical Insulation, IEEE Transactions on* 16.2 (Apr. 2009), pp. 489–494.

[3] S. O. Ahmedou and M. Havet. “Effect of process parameters on the EHD airflow”. In: *Journal of Electrostatics* 67 (2009), pp. 222–227.

[4] S. O. Ahmedou, M. Havet, and O. Rouaud. “Assessment of the Electrohydrodynamic Drying Process”. In: *Food and Bioprocess Technology* 2.3 (Sept. 2009), pp. 240–247.

[5] A. Aliat, C. T. Hung, C. J. Tsai, and J. S. Wu. “Implementation of Fuchs’ model of ion diffusion charging of nanoparticles considering the electron contribution in dc-corona chargers in high charge densities”. In: *Journal of Physics D: Applied Physics* 42 (2009), pp. 1–9.

[6] P. H. G. Allen and T. G. Karayiannis. “Electrohydrodynamic enhancement of heat transfer and fluid flow”. In: *Heat Recovery Systems & CHP* 15.5 (1995), pp. 389–423.

[7] P. Atten, A. Adamiak, B. Khaddoura, and J. L. Coulomb. “Simulation of corona discharge in configurations with a sharp electrode”. In: *Journal of Optoelectronics and Advanced Materials* 6.3 (Sept. 2004), pp. 1023–1028.

[8] L. V. Ballestra and R. Sacco. “Numerical problems in semiconductor simulation using the hydrodynamic model: A second-order finite difference scheme”. In: *Journal of Computational Physics* 195.1 (2004). cited By (since 1996) 4, pp. 320–340.

[9] A.J. Bard and L.R. Faulkner. *Electrochemical methods: fundamentals and applications*. 2nd ed. Wiley New York, 1980.

[10] M. I. Boulos, P. Fauchais, and E. Pfender. *Thermal plasmas: fundamentals and applications*. The Language of science. Plenum Press, 1994.

[11] G. S. P. Castle, I. I. Inculet, and K. I. Burgess. “Ozone Generation in Positive Corona Electrostatic Precipitators”. In: *IEEE Transactions on Industry and General Applications* IGA-5.4 (July 1969), pp. 489–496.

[12] J. S. Chang, H. Tsubone, Y. N. Chun, A. A. Berezin, and K. Urashima. “Mechanism of electrohydrodynamically induced flow in a wire-non-parallel plate electrode type gas pump”. In: *Journal of Electrostatics* 67.2-3 (2009). 11th International Conference on Electrostatics, pp. 335–339.

[13] J. S. Chang, J. Ueno, H. Tsubone, G. D. Harvel, S. Minami, and K. Urashima. “Electrohydrodynamically induced flow direction in a wire-non-parallel plate electrode corrona discharge”. In: *Journal of Physics D: Applied Physics* 40 (2007), pp. 5109–5111.

[14] B. Chini, J. W. Jerome, and R. Sacco. “Multi-physics modeling and finite element approximation of charge flow in ionic channels”. In: *Thermal, Mechanical and Multiphysics Simulation and Experiments in Micro-Electronics and Micro-Systems, 2006. EuroSime 2006. 7th International Conference on*. IEEE. 2006, pp. 1–8.

[15] T. Christen and M. Seeger. “Simulation of unipolar space charge controlled electric fields”. In: *J. Electrostatics* 65 (2007), pp. 11–20.

[16] J. S. Cotton, A. J. Robinson, M. Shoukri, and J. S. Chang. “AC Voltage Induced Electrohydrodynamic Two-Phase Convective Boiling Heat Transfer in Horizontal Annular Channels”. In: *Experimental Thermal and Fluid Science* 41 (2012), pp. 31–42.

[17] L. C. Evans. *Partial Differential Equations*. Providence: American Mathematical Society, 2010.

[18] R. Eymard, T. Gallouet, and R. Herbin. *Finite Volume Methods*. Ed. by P. G. Ciarlet and J. L. Lions. Vol. 7. Handbook of Numerical Analysis. Marseille: Elsevier BV, 1997, pp. 713–1020.

[19] C. de Falco, J. W. Jerome, and R. Sacco. “Quantum-corrected drift-diffusion models: Solution fixed point map and finite element approximation”. In: *J. Comp. Ph.* 228.5 (2009), pp. 1770–1789.

[20] C. a b de Falco, R. c Sacco, and G. d Scrofani. “Stabilized 3D finite elements for the numerical solution of the Navier-Stokes equations in semiconductors”. In: *Computer Methods in Applied Mechanics and Engineering* 196.9-12 (2007). cited By (since 1996) 4, pp. 1729–1744.

[21] J. H. Ferziger and M. Perić. *Computational Methods for Fluid Dynamics*. Springer, 1996.

[22] T. S. Fisher, S. V. Garimella, D. B. Go, and R. K. Monja. “Various methods, apparatuses, and systems that use ionic wind to affect heat transfer”. Patent US 7545640. June 2009.

[23] C. Geuzaine and J. F. Remacle. *Gmsh: a three-dimensional finite element mesh generator with built-in pre- and post-processing facilities*. URL: `http://geuz.org/gmsh`.

[24] D. B. Go, S. V. Garimella, and T. S. Fisher. “Ionic winds for locally enhanced cooling”. In: *Journal of Applied Physics* 102 (2007), p. 053302.

[25] D. B. Go, S. V. Garimella, and T. S. Fisher. “Numerical Simulation of Microscale Ionic Wind for Local Cooling Enhancement”. In: *Thermal and Thermomechanical Phenomena in Electronics Systems, 2006. ITHERM ’06. The Tenth Intersociety Conference on*. June 2006, pp. 45–53.

[26] D. B. Go, S. V. Garimella, T. S. Fisher, and V. Bahadur. “Planar microscale ionization devices in atmospheric air with diamond-based electrodes”. In: *Plasma Sources Science and Technology* 18.3 (2009), p. 035004.

[27] D. B. Go, R. A. Maturana, T. S. Fisher, and S. V. Garimella. “Enhancement of external forced convection by ionic wind”. In: *International Journal of Heat and Mass Transfer* 51 (2008), pp. 6047–6053.

[28] B. Gschaider. *swak4Foam*. URL: `http://openfoamwiki.net/index.php/Contrib/swak4Foam`.

[29] K. Honer. *Silent air-cooling technology: a solution to the cooling quandary?* 2010. URL: `http://www.tessera.com/abouttessera/pressroom/Documents/Electronic\_Products\_May\_2010.pdf`.

[30] C. P. Hsu, N. E. Jewell-Larsen, I. A. Krichtafovitch, S. W. Montgomery, J. T. Dibene II, and A. V. Mamishev. “Miniaturization of electrostatic fluid accelerators”. In: *Journal of Microelectromechanical Systems* 16.4 (Aug. 2007), pp. 809–815.

[31] Ren-Tsung Huang, Wen-Jenn Sheu, and Chi-Chuan Wang. “Heat transfer enhancement by needle-arrayed electrodes – An EHD integrated cooling system”. In: *Energy Conversion and Management* 50.7 (2009), pp. 1789–1796.

[32] J. W. Jerome, B. Chini, M. Longaretti, and R. Sacco. “Computational modeling and simulation of complex systems in bio-electronics”. In: *Journal of Computational Electronics* 7.1 (2008), pp. 10–13.

[33] J. W. Jerome and R. Sacco. “Global weak solutions for an incompressible charged fluid with multi-scale couplings: Initial-boundary-value problem”. In: *Nonlinear Analysis : Th. , Met. & Ap.* 71.12 (2009), e2487–e2497.

[34] J.W. Jerome. *Analysis of charge transport: a mathematical study of semiconductor devices*. Springer-Verlag, 1996.

[35] N. E. Jewell-Larsen, C. P. Hsu, I. A. Krichtafovitch, S. W. Montgomery, J. T. Dibene II, and A. V. Mamishev. “CFD Analysis of electrostatic fluid accelerators for forced convection cooling”. In: *IEEE Transactions on Dielectrics and Electrical Insulation* 15.6 (Dec. 2008), pp. 1745–1753.

[36] N. E. Jewell-Larsen, S. V. Karpov, I. A. Krichtafovitch, V. Jayanty, C. P. Hsu, and A. V. Mamishev. “Modeling of corona-induced electrohydrodynamic flow with COMSOL multiphysics”. In: *Proc. ESA Annual Meeting on Electrostatics*. Minneapolis, MN, June 2008, pp. 1–13.

[37] N. E. Jewell-Larsen, H. Ran, Y. Zhang, M. Schwiebert, and A. V. Mamishev. “Electrohydrodynamic (EHD) Cooled Laptop”. In: *Proc. Semiconductor Thermal Measurement and Management Symp. (SEMI-THERM)*. San Jose, CA USA, Mar. 2009, pp. 1–7.

[38] N. E. Jewell-Larsen, E. Tran, I. A. Krichtafovitch, and A. V. Mamishev. “Design and optimization of electrostatic fluid accelerators”. In: *IEEE Transactions on Dielectrics and Electrical Insulation* 13.1 (Feb. 2006), pp. 191–203.

[39] N. E. Jewell-Larsen, P. Q. Zhang, C. P. Hsu, I. A. Krichtafovitch, and A. V. Mamishev. “Coupled-Physics Modeling of Electrostatic Fluid Accelerators for Forced Convection Cooling”. In: *9th AIAA/ASME Joint Thermophysics and Heat Transfer Conference*. 2006.

[40] T. B. Jones. “Electrohydrodynamically enhanced heat transfer in liquids-A review”. In: *Advances in Heat Transfer* 14 (1979), pp. 107–149.

[41] N. A. Kaptsov. *Elektricheskie Yavleniya v Gazakz i Vakuume*. Moscow: OGIZ, 1947.

[42] S. Karpov and I. Krichtafovitch. “Electrohydrodynamic flow modelling using FEMLAB”. In: *Proc. COMSOL conference*. Boston, MA, 2005, pp. 399–403.

[43] N. Kasayapanand. “Enhanced heat transfer in inclined solar chimneys by electrohydrodynamic technique”. In: *Renewable Energy* 33 (2008), pp. 444–453.

[44] N. Kasayapanand and T. Kiatsiriroat. “EHD enhanced heat transfer in wavy channel”. In: *Int. Communications in Heat and Mass Transfer* 32 (2005), pp. 809–821.

[45] N. Kasayapanand and T. Kiatsiriroat. “Numerical modeling of the electrohydrodynamic effect to natural convection in vertical channels”. In: *Int. Communications in Heat and Mass Transfer* 34.2 (2006), pp. 162–175.

[46] L. Keesey. *NASA is Making Hot, Way Cool*. URL: `http://www.nasa.gov/topics/technology/features/thermal-control-tech.html`.

[47] C. Kim, D. Park, K. C. Noh, and J. Hwang. “Velocity and energy conversion efficiency characteristics of ionic wind generator in a multistage configuration”. In: *Journal of Electrostatics* 68 (2010), pp. 36–41.

[48] L. B. Loeb. *Fundamental processes of electrical discharge in gases*. John Wiley & Sons, 1939.

[49] M. Longaretti, B. Chini, J. W. Jerome, and R. Sacco. “Electrochemical modeling and characterization of voltage operated channels in nano-bio-electronics”. In: *Sensor Letters* 6.1 (2008), pp. 49–56.

[50] M. Longaretti, G. Marino, B. Chini, J. W. Jerome, and R. Sacco. "Computational models in nano-bioelectronics: Simulation of ionic transport in voltage operated channels". In: *Journal of Nanoscience and Nanotechnology* 8.7 (2008), pp. 3686–3694.

[51] A. K. M. Mazumder and F. C. Lai. "Two-Stage Electrohydrodynamic Gas Pump in a Square Channel". In: *Proc. ESA Annual Meeting on Electrostatics 2011*. 2011.

[52] A. K. M. Mazumder, F. C. Lai, and X. B. Zhao. "Effects of Grounded Electrodes Size on the Performance of EHD Gas Pump in a Square Channel". In: *Proc. ESA Annual Meeting on Electrostatics 2011*. 2011.

[53] *McMaster University Thermal Management Research Laboratory*. URL: `http://tmrl.mcmaster.ca/facilities.html`.

[54] E. Moreau and G. Touchard. "Enhancing the mechanical efficiency of electric wind in corona discharges". In: *Journal of Electrostatics* 66 (2008), pp. 39–44.

[55] R. Morrow. "The theory of positive glow corona". In: *Journal of Physics D: Applied Physics* 30.22 (1999), p. 3099.

[56] K. Ng, C. Y. Ching, and J. S. Cotton. "Transient Two-Phase Flow Patterns by Application of a High Voltage Pulse Width Modulated Signal and the Effect on Condensation Heat Transfer". In: *Journal of heat transfer* 133.9 (2011), p. 091501.

[57] *OpenFOAM® - The Open Source Computational Fluid Dynamics (CFD) Toolbox*. URL: `http://www.openfoam.com`.

[58] F. W. Peek. *Dielectric Phenomena in High Voltage Engineering*. New York: McGraw-Hill, 1929.

[59] A. Prohl. *Projection and Quasi-Compressibility Methods for Solving the Incompressible Navier-Stokes Equations*. Stuttgart: B. G. Teubner, 1997.

[60] A. Quarteroni, F. Saleri, and A. Veneziani. “Factorization methods for the numerical approximation of Navier-Stokes equations”. In: *Computer Methods in Applied Mechanics and Engineering* 188.1-3 (2000), pp. 505–526.

[61] I. Rubinstein. *Electro-diffusion of ions*. Vol. 11. SIAM, 1990.

[62] R.J. Ryham. “Existence, uniqueness, regularity and long-term behavior for dissipative systems modeling electrohydrodynamics”. In: *arXiv preprint arXiv:0910.4973* (2009).

[63] R.J. Ryham. “Global existence and long term behavior of 2d electro-hydrodynamics”. In: *arXiv preprint arXiv:0810.2064* (2008).

[64] P. Sattari, G. S. P. Castle, and K. Adamiak. “FEM-FCT based dynamic simulation of corona discharge in point-plane configuration”. In: *2009 Electrostatics Joint Conference*. Boston University, MA, USA, June 2009.

[65] P. Sattari, G. S. P. Castle, and K. Adamiak. “FEM-FCT-Based Dynamic Simulation of Corona Discharge in Point-Plane Configuration”. In: *Industry Applications, IEEE Transactions on* 46.5 (Sept. 2010), pp. 1699–1706.

[66] A.E. Seaver. “Onset potential for unipolar charge injection”. In: *Industry Applications Society Annual Meeting, 1993., Conference Record of the 1993 IEEE*. IEEE. 1993, pp. 1605–1610.

[67] S. Siedel, S. Cioulachtjian, Robinson A. J., and J. Bonjour. “Electric field effects during nucleate boiling from an artificial nucleation site”. In: *Experimental Thermal and Fluid Science* 35 (5 2011), pp. 762–771.

[68] J. A. Stratton. *Electromagnetic Theory*. McGraw Hill, 1941.

[69] J. J. Thomson. “Conduction of Electricity trough Gases, 2nd Edition”. In: Cambridge University Press, 1911, 490 ff.

[70] J. S. Townsend. *Electricity in Gases*. Clarendon Press, 1915, p. 331.

[71] J. S. Townsend. “The Conductivity produced in Gases by the Motion of Negatively-charged Ions”. In: *Nature* 62.1606 (1900), pp. 340–41.

[72] J. S. Townsend. “The Conductivity produced in gases by the motion of negatively charged ions”. In: *Philosophical Magazine* 1.2 (1901), pp. 198–227.

[73] H. Tsubone, J. Ueno, B. Komeili, S. Minami, G. D. Harvel, K. Urashima, C. Y. Ching, and J. S. Chang. “Flow characteristics of dc wire-non-parallel plate electrohydrodynamic gas pumps”. In: *Journal of Electrostatics* 66 (2008), pp. 115–121.

[74] A. Yabe, Y. Mori, and K. Hijikata. “EHD study of the corona wind between wire and plate electrodes”. In: *AIAA Journal* 16.4 (1978), pp. 340–345.

[75] Z. Yu, R. K. Al-Dadah, and R. H. S. Winterton. “A theoretical investigation of electrohydrodynamically (EHD) enhanced condensation heat transfer”. In: *Proc. Int. Conf. Two-Phase Modelling and Experimentation*. Vol. 1. Pisa, Italy, 1999, pp. 463–72.

[76] J Zhang and F. C. Lai. “Effect of emitting electrode number on the performance of EHD gas pump in a rectangular channel”. In: *Proc. ESA Annual Meeting on Electrostatics 2010*. 2010.

[77] L. Zhao and K. Adamiak. “EHD flow produced by electric corona discharge (numerical and experimental studies, and applications)”. In: *2009 Electrostatics Joint Conference*. Boston University, MA, USA, June 2009.